

Explosive Nucleosynthesis in Near-Chandrasekhar-mass White Dwarf Models for Type Iax Supernovae: Dependence on Model Parameters

SHING-CHI LEUNG^{1,2} AND KEN'ICHI. NOMOTO¹

¹*Kaoli Institute for the Physics and Mathematics of the Universe (WPI), The University of Tokyo Institutes for Advanced Study, The University of Tokyo, Kashiwa, Chiba 277-8583, Japan*

²*TAPIR, Walter Burke Institute for Theoretical Physics, Mailcode 350-17, Caltech, Pasadena, CA 91125, USA*

(Dated: July 20, 2020)

ABSTRACT

The recently observed diversity of Type Ia supernovae (SNe Ia) has motivated us to conduct the theoretical modeling of SNe Ia for a wide parameter range. In particular, the origin of Type Iax supernovae (SNe Iax) has been obscure. Following our earlier work on the parameter dependence of SN Ia models, we focus on SNe Iax in the present study. For a model of SNe Iax, we adopt the currently leading model of pure turbulent deflagration (PTD) of near-Chandrasekhar mass C+O white dwarfs (WDs). We carry out 2-dimensional hydrodynamical simulations of the propagation of deflagration wave, which leaves a small WD remnant behind and eject nucleosynthesis materials. We show how the explosion properties, such as nucleosynthesis and explosion energy, depend on the model parameters such as central densities and compositions of the WDs (including the hybrid WDs), and turbulent flame prescription and initial flame geometry. We extract the associated observables in our models, and compare with the recently discovered low-mass WDs with unusual surface abundance patterns and the abundance patterns of some SN remnants. We provide the nucleosynthesis yield tables for applications to stellar archaeology and galactic chemical evolution. Our results are compared with the representative models in the literature.

Keywords: (stars:) supernovae: general – hydrodynamics – nuclear reactions, nucleosynthesis, abundances – (stars:) white dwarfs – supernova remnants

1. INTRODUCTION

1.1. *Type-Ia Supernovae Physics*

Type Ia supernova (SN Ia) is important in the cosmological and chemical context. Their standardized light curves with Phillip's relation (Phillips 1993) lead to the use of SNe Ia as standard candles and the discovery of cosmic acceleration and its implications of dark energy (Riess et al. 1996; Perlmutter et al. 1997). SNe Ia are also the major channel for iron-peak element production (e.g., Nomoto & Leung 2017a). The role of SN Ia can be seen in the galactic chemical evolution, including the $[\alpha/\text{Fe}]$ versus $[\text{Fe}/\text{H}]$ relation (Nomoto et al. 2013) and the $[\text{Mn}/\text{Fe}]$ versus $[\text{Fe}/\text{H}]$ relation (Seitenzahl et al. 2013; Leung & Nomoto 2020; Kobayashi et al. 2020).

The diversified observational properties of SNe Ia (e.g., Li et al. 2001; Foley et al. 2016; Taubenberger 2017; Jiang et al. 2018) suggest the multiple explosion mechanisms (see, e.g., Hoeflich 2017; Röpke 2017; García-Berro & Lorén-Aguilar 2017; Pakmor 2017; Nomoto & Leung 2017a, for recent reviews).

In our earlier work with 2-dimensional hydrodynamical simulations, we have studied the turbulent deflagration model with or without deflagration-detonation transition (DDT) for the near-Chandrasekhar mass C+O white dwarfs (WDs) (Leung & Nomoto 2018) and the double detonation (DD) models for both sub-Chandrasekhar mass WDs and near-Chandrasekhar mass WDs (Leung & Nomoto 2020). We have shown how the explosion properties, such as nucleosynthesis, explosion energy, and asphericity, depend on the model parameters of the flame and WDs.

In the present work, we focus on Type Iax supernovae (SNe Iax) (e.g., Jha 2017, for a review). A few well observed SNe Iax are SN 2002cx (e.g. Li et al. 2003), SN 2005hk (e.g., Phillips et al. 2007), SN 2008ha (e.g., Foley et al. 2009) and SN 2014dt (Kawabata et al. 2018). SNe Iax are peculiar SNe Ia, having lower luminosities as well as lower ejecta velocities and masses than normal SNe Ia, Moreover, SNe Iax show quite a large variation of light curve and ejecta properties. SNe

Iax are peculiar but may not be rare, as indicated by its statistics. It contributes to $\sim 10\%$ of the SN Ia population (Li et al. 2001).

Among the various proposed models, we adopt a pure deflagration model, which has been shown to be a promising model to explain the main properties of SNe Iax (e.g., Branch et al. 2004; Phillips et al. 2007; Sahu et al. 2008; Foley et al. 2009; Jordan et al. 2012; Kromer et al. 2013; Fink et al. 2014). The outcome of the pure deflagration depends mainly on the subsonic flame speed (e.g., Nomoto et al. 1976, 1984; Gamezo et al. 2004; Röpke et al. 2007; Jordan et al. 2012; Fink et al. 2014), and the weak explosions with low kinetic energy and small production of ^{56}Ni can be consistent with the observed properties of SNe Iax.

In our earlier works on the hydrodynamics and nucleosynthesis of SNe Ia (Leung & Nomoto 2018, 2020), we have shown that the abundance pattern of nucleosynthesis yields are important to constrain the supernova model from the light curves and spectra. In the present study, we perform 2-dimensional (2-D) simulations of PTD and calculate nucleosynthesis for near-Chandrasekhar mass WDs with various parameters such as composition (C+O and C+O+Ne) and central densities of WDs and flame physics such as initial flame geometry.

We provide tables of our nucleosynthesis yields, and compare them with the unusual abundance patterns of some WDs and SN remnants to infer their origins. Our results could be important to the chemical evolution of some dwarf spheroidal galaxies (dSphs). In Kobayashi et al. (2015), the SN Iax model can be an explanation to the early drop in $[\text{O}/\text{Fe}]$ and the early rise in $[\text{Mn}/\text{Fe}]$ relations.

In section 2, we describe the progenitor stars and WDs, and briefly review the methods and input physics to calculate the PTD. In section 3, we present typical hydrodynamical and thermodynamical properties of the PTD models. We investigate how the chemical yields of SNe Iax change with the model parameters. We compare our yields with some metal-enriched low-mass WDs and SNRs. and discuss its application to chemical evolution of galaxies.

2. INITIAL MODELS AND INPUT PHYSICS

2.1. Initial Models

We first construct an isothermal WD in hydrostatic equilibrium with a central density ρ_c , temperature T_{ini} and metallicity Z . In the equation of state, Coulomb effects are taken into account. The characteristic model described in the next section assumes a C+O WD of mass $1.37 M_{\odot}$ with a central density $3 \times 10^9 \text{ g cm}^{-3}$

and solar metallicity. In the simulation solar metallicity is represented by the characteristic isotope ^{22}Ne with the mass fraction of $X(^{22}\text{Ne}) = 0.025$ (Nomoto et al. 1984; Leung & Nomoto 2018). The composition is different from the detailed solar composition (Asplund et al. 2009). However, we remark that the nucleosynthesis results are insensitive to the exact representation because the nucleosynthesis depends primarily on the electron mole fraction Y_e of the burnt matter, which is dominated by electron capture after the matter is swept by the deflagration wave. The initial electron mole fraction and composition play much smaller roles unlike the canonical deflagration with deflagration-detonation transition due to the lack of nucleosynthesis by detonation at low densities.

Such a C+O WD is assumed to be formed in the single degenerate channel of binary evolution (e.g., Nomoto 1982a; Nomoto & Leung 2017a, 2018). Thus the central density of the WD mainly depends on the accretion rate. It also depends on the spin of the white dwarf (e.g., Benvenuto et al. 2015) for which the central density at the deflagration is as high as $5 - 6 \times 10^9 \text{ g cm}^{-3}$ and even higher depending on the time scale of the angular momentum loss. Thus we parametrized the central density.

We also consider possible hybrid WDs as demonstrated by Denissenkov et al. (2013). Here carbon is ignited in the outer layer of the C+O core of near $\sim 10 M_{\odot}$ star during its AGB phase (e.g., Nomoto 1984). If the carbon flame propagates through the center, the C+O core is converted into an O+Ne+Mg core (e.g., Nomoto 1987; Nomoto & Leung 2017b). However, if the overshooting of convection across the carbon-flame down to the C+O layer is large, it would reduce the nuclear fuel to prevent the carbon-flame from propagation to the center (see, however, e.g., Lecoanet et al. 2016; Brooks et al. 2017). Then the degenerate core is composed of C+O in the central region and O+Ne+Mg in the outer layer, where the composition changes at a designed transition mass M_{core} .

When such a core becomes a WD, it is called a hybrid WD. When the mass of the hybrid WD becomes close to the near-Chandrasekhar limit, carbon is ignited in the central region which produces a convection zone. During the simmering phase, the convection would mix the central C+O core and the outer O+Ne+Mg layer before the deflagration is initiated. It produces a WD made of C+O+Ne mixture.

In the present study, we assume that such hybrid WD is formed and the C+O-rich core is completely mixed with the outer O+Ne-rich envelope for simplicity. After mixing during the simmering phase, we assume that the

WD has a uniform composition with the mass fractions of ^{12}C , ^{16}O , and ^{20}Ne are 0.2, 0.5, and 0.3 for simplicity (Kromer et al. 2015) and in view of the uncertainties in the overshooting parameter. The effect of metallicity is included by combining the above composition with ^{22}Ne as the key isotope for metallicity.

If the carbon burning reaches the center, the WD becomes an oxygen-neon-magnesium (O+Ne+Mg) WD. These WDs undergo electron capture and are very likely collapse to form neutron stars (Zha et al. 2019; Leung et al. 2019). For a possible case of partial mass ejection, the nucleosynthesis yields are given in Appendix C.

2.2. Methods and Input Physics

For the adopted initial models of the WDs, we perform two-dimensional hydrodynamics simulations of the propagation of the PTD by specifying the initial deflagration structure by hand.

Deflagration (Nomoto et al. 1976; Nomoto 1982b; Timmes & Woosley 1992; Niemeyer & Woosley 1997; Woosley 1997) is the nuclear flame, where thermonuclear runaway takes place with a timescale shorter than the dynamical timescale. The flame propagates at a sub-sonic speed by energy transport across the flame due to electron conduction and convection as described below (e.g., Nomoto & Leung 2017b,a; Leung & Nomoto 2017a, 2019; Leung et al. 2020).

Deflagration is subject to hydrodynamical instabilities including Rayleigh-Taylor (RT) instabilities, Kelvin-Helmholtz (KH) instabilities and Landau-Darrieus (LD) instabilities present during its propagation (e.g., Timmes 1992; Livne & Arnett 1993; Niemeyer & Hillebrandt 1995; Röpke et al. 2004a,b; Bell et al. 2004a,b). The flame width ($\sim 10^{-6} - 10^{-3}$ cm) is in general much smaller than that resolved by simulation (e.g., Timmes & Woosley 1992; Niemeyer et al. 1995). Special flame front tracking technique, such as the level-set method, (Osher & Sethian 1988), is necessary for a consistent description of the interaction between flame and the dynamics (Reinecke et al. 1999b). Sub-grid scale turbulence model is often necessary (Clement 1993; Schmidt et al. 2006). The flame structure is coupled with turbulence, where the turbulent motion emerges in the length scale down to the Kolmogorov scale. Eddy motions can alter the deflagration front by fluid advection above the Gibson's scale. Below that scale, the irregularities are polished (e.g., Niemeyer et al. 1995; Jackson et al. 2014). Early multi-dimensional realizations have been done in (e.g., Reinecke et al. 1999a, 2002a,b; Röpke et al. 2004a,b; Röpke & Hillebrandt 2005; Röpke 2005; Röpke et al. 2006a,b).

The turbulent deflagration is tracked by the level-set method (Osher & Sethian 1988; Reinecke et al. 1999b) with the sub-grid turbulence scheme given in Clement (1993); Niemeyer et al. (1995). The turbulent flame formula used the analytical results in Pocheau (1994). The connections between the local turbulence strength and the effective turbulent flame propagation speed are taken from Schmidt et al. (2006), but with variations shown in Hicks (2015). DDT is artificially suppressed throughout the simulation.

Our simulation code is a general hydrodynamics code embedded with supernova physics (Leung et al. 2015). This code has been applied to previous SN Ia parameter surveys for the near-Chandrasekhar mass WDs (Leung & Nomoto 2017b, 2018) and also sub-Chandrasekhar mass WDs (Leung & Nomoto 2020). The code has been recently extended to study other types of supernova, including the electron capture supernova (Leung et al. 2020) and jet-driven supernova (Tsuruta et al. 2018). The simulation code uses a simplified 7-isotope network (Timmes et al. 2000) to trace the isotopic abundances and a three-step burning network (Townesley et al. 2002) to mimic the nuclear reactions in deflagration.

In the three-step burning scheme, the fast reaction of carbon-burning is controlled by the level-set method. The advanced burning and O-burning are set to be dependent on the corresponding burning timescales (Calder et al. 2007). For matter with a sufficiently high density ($> 10^8$ g cm $^{-3}$) and temperature ($> 5 \times 10^9$ K) such that the matter is burnt in nuclear statistical equilibrium (NSE), electron captures take place. The corresponding rates for the matter in the NSE are computed by summing up the individual rates of many isotopes included in the nuclear reaction network used by the post-processing. Updated weak interaction rates are obtained from the literature including Nabi & Klapdor-Kleingrothaus (2004); Seitzzahl et al. (2009). We refer the further details in Appendix A.

Pure deflagration cannot completely unbind the star if the flame is quenched early by the WD expansion (Nomoto et al. 1976; Livne 1993). Its sub-sonic nature provides sufficient time for electron capture to take place before the WD expands (e.g., Iwamoto et al. 1999; Seitzzahl et al. 2009), which is a key to produce neutron-rich isotopes in the ejecta. Such conditions are hardly achieved by other types of SNe.

After the hydrodynamical simulations, we use the thermodynamics history of the tracer particles to reconstruct the detailed nucleosynthesis (Travaglio et al. 2004; Seitzzahl et al. 2009; Townesley et al. 2016).

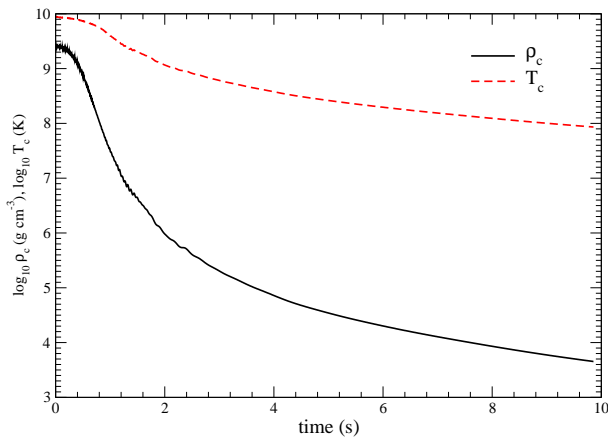


Figure 1. Central density (black dashed line) and central temperature (red dashed line) against time for the characteristic model.

3. CHARACTERISTIC MODEL FOR SN IAX

We first examine the typical behaviour of the SN Iax based on the C+O WD as described in Section 2. Then, we examine the stellar properties, thermodynamics, energetics and chemical properties. A central flame $c3$ (corresponding to three-finger, see Reinecke et al. (1999a) for illustrations) is placed at the beginning.

3.1. Thermodynamics

In Figure 1 we plot the central density (black dashed line) and the central temperature (red dashed line) of the characteristic model as a function of time. After the core is burnt, the core remains static for the first 0.2 s. Afterwards, it expands and the central density drops by 2 orders of magnitude in the first 2 s. Then the core expansion slows down. It reaches an asymptotic value $\sim 10^{4.5}$ g cm $^{-3}$ beyond 8 s, showing that the core stops expanding because it has transferred all its momentum to the outer material, which has a relatively lower density and hence smaller inertia to be ejected. The temperature shows a similar evolution but with a difference that the core temperature continues to drop even at the end of simulation. The temperature is too low for any important nuclear reactions to take place after it has left NSE (defined at $T > 5 \times 10^9$ K), which occurs at ~ 1 s after explosion.

To further clarify the effects of nuclear reactions in the star, we plot in Figure 2 the tracer particle summary. In this figure, for each tracer particle we search for its maximum density and temperature achieved in the simulations, and then we bin them into different temperature ranges. The variety of particle maximum density within the same temperature range is represented by the "error bars" in the figure. Notice that for SN Iax, the maxi-

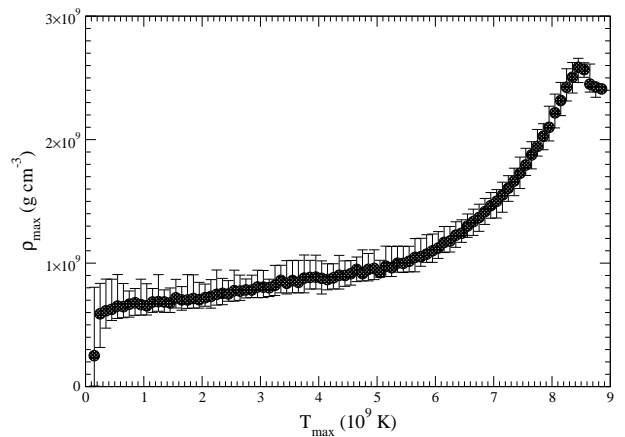


Figure 2. The maximum density against maximum temperature for the characteristic model using the thermodynamics history of the tracer particles. The error bars and the data points correspond to the range of density and the mean density of the tracer particles obtained in the thermodynamics history.

mum ρ_c and T_c are obtained at the same time because there is no shock wave triggered in the event.

There are two groups of the particles developed in the simulation. The first group corresponds to the particle which is directly burnt, this consists of particles with $\rho_{\max} > \sim 6 \times 10^9$ K. There is a monotonic relation between ρ_{\max} and T_{\max} and the fluctuation is very small. The star remains close to static and the asymmetry of the deflagration wave is not large enough to create significant time difference for burning matter near the same radius. The second group corresponds to the particles being burnt by the deflagration wave but after the star has expanded and the flame becomes aspherical. Matter with the same ρ_{\max} can have different T_{\max} . This means that they have the same initial density but they experience different levels of expansion before the deflagration arrives.

3.2. Energetics

In Figure 3 we plot the energy production rate against time for the characteristic model. The energy production rate is defined by $\Delta Q/\Delta t$, where ΔQ is the amount of energy gained by the system through nuclear reaction at that current step with a time step size Δt . The amount of energy, as described in Section 2, is done by the level-set methods coupled with our simplified network.

In the first 0.4 s, the system releases energy mainly by nuclear deflagration. The energy production rate is low, $\sim 10^{50}$ erg s $^{-1}$. After that from 0.4 s to 1 s, the energy production switches to advance burning and NSE burning when the density at the deflagration front becomes low ($\sim 10^7$ g cm $^{-3}$). The energy production rate is high

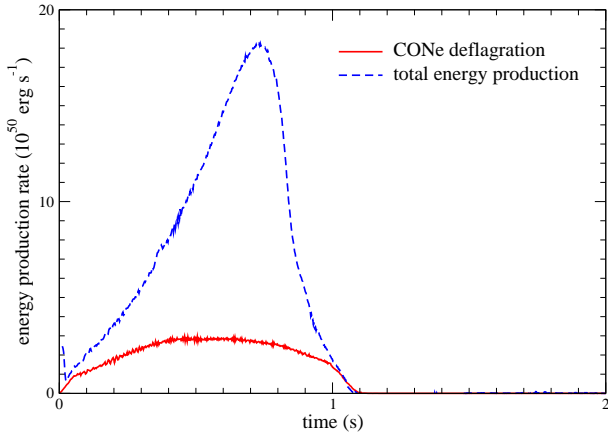


Figure 3. The energy production rate (black solid line) and its component (red dashed line) against time for the characteristic model. Here, the energy production rate by CONe deflagration is extracted for comparison.

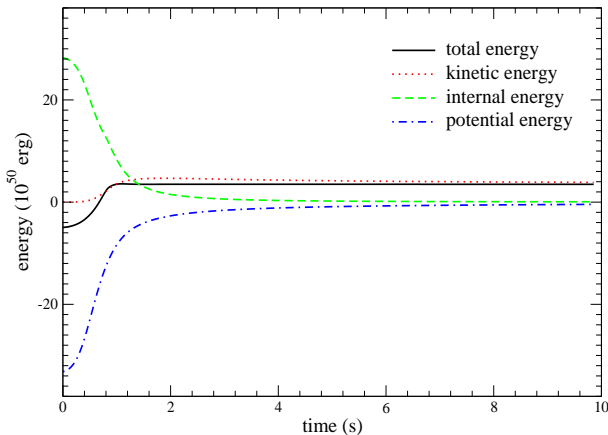


Figure 4. The total energy (black solid line), kinetic energy (red dotted line), internal energy (green dashed line) and gravitational energy (blue long dashed line) against time for the characteristic model.

and reach $\sim 10^{51} \text{ erg s}^{-1}$ at maximum. At that time nuclear deflagration no longer produces any observable amount of energy. We remark that different from standard SNe Ia, there can be enhancement from mixing of fresh ^{16}O and ^{20}Ne into the ash when the ash expands.

In Figure 4 we also plot the energy evolution similar to Figure 3. The total energy, kinetic, internal and potential energy are plotted.

Similar to the energy production rate, the total energy quickly rises at the beginning and reaches its equilibrium value at ~ 1 s after the flame has propagated. When the expansion quenches the flame and cools down the ash, the total energy no longer changes. The kinetic energy shows a similar behaviour but with a small bump about 1.3 s. This is because during the expansion of the flame,

it creates non-local acceleration of matter, especially the hot matter.

The total internal energy on the contrary is dominated by the initial internal energy. It constantly decreases, showing that the star expands and loses energy through its expansion work done. Unlike SN Ia, it has no bump in its evolution, which means that the flame does not produce any significant shock compression to the matter, including the low-density matter on the surface. This is consistent with the idea that the deflagration is subsonic. The system has always sufficient time to adjust its structure to accommodate the energy input by nuclear burning. It reaches its asymptotic energy ~ 0 beyond 3 s.

For the gravitational energy, since there is no contraction during the whole evolution, it first quickly rises in the first 2 s, and then it approaches its asymptotic value near zero, slowly as the star expands. But it reaches its asymptotic value much slower than the internal energy, showing that the system is expanding much slower than ordinary SNe Ia.

3.3. Flame Propagation

In Figure 5 we plot the flame structure of our representative model from the beginning to 2.5 s at an interval of 0.5 s. We use the *c3* flame which we have applied in previous SNe Ia surveys. This flame mimics and promotes the early growth of RT instabilities. We note that putting spherical flame at the center can give enhanced flame propagation along the symmetry axis, while the WD does not have a preferred direction due to its static initial profile. Therefore, to avoid the development of such unphysical structure, we use the *c3* flame so that the off-axis flame development dominates the growth of flame.

We also simulate PTD in the hybrid WD which is composed of C+O+Ne matter. At 0.5 s the flame only burns the innermost ~ 200 km of the star. One of the "finger" features near the y -axis is suppressed, while the other two "fingers" continue to grow further. The curly colour pattern in its temperature distribution demonstrates the turbulent motion inside the ash at 1.5 s. At that time the flame has already cooled down to about $\sim 5 \times 10^9$ K. After that, both NSE burning and nuclear deflagration no longer supply extra energy. The star gradually expands. The peak temperature reaches $\sim 3 \times 10^9$ K at 2.0 s and $\sim 2 \times 10^9$ K at 2.5 s. From 2.0 s onward, when the flame expands upwards due to its buoyancy, the unburned matter floats downward to fill up the space. The opposite direction of the flow current creates the KH instability, where the curly structure can be seen along the "fingers". On top of the

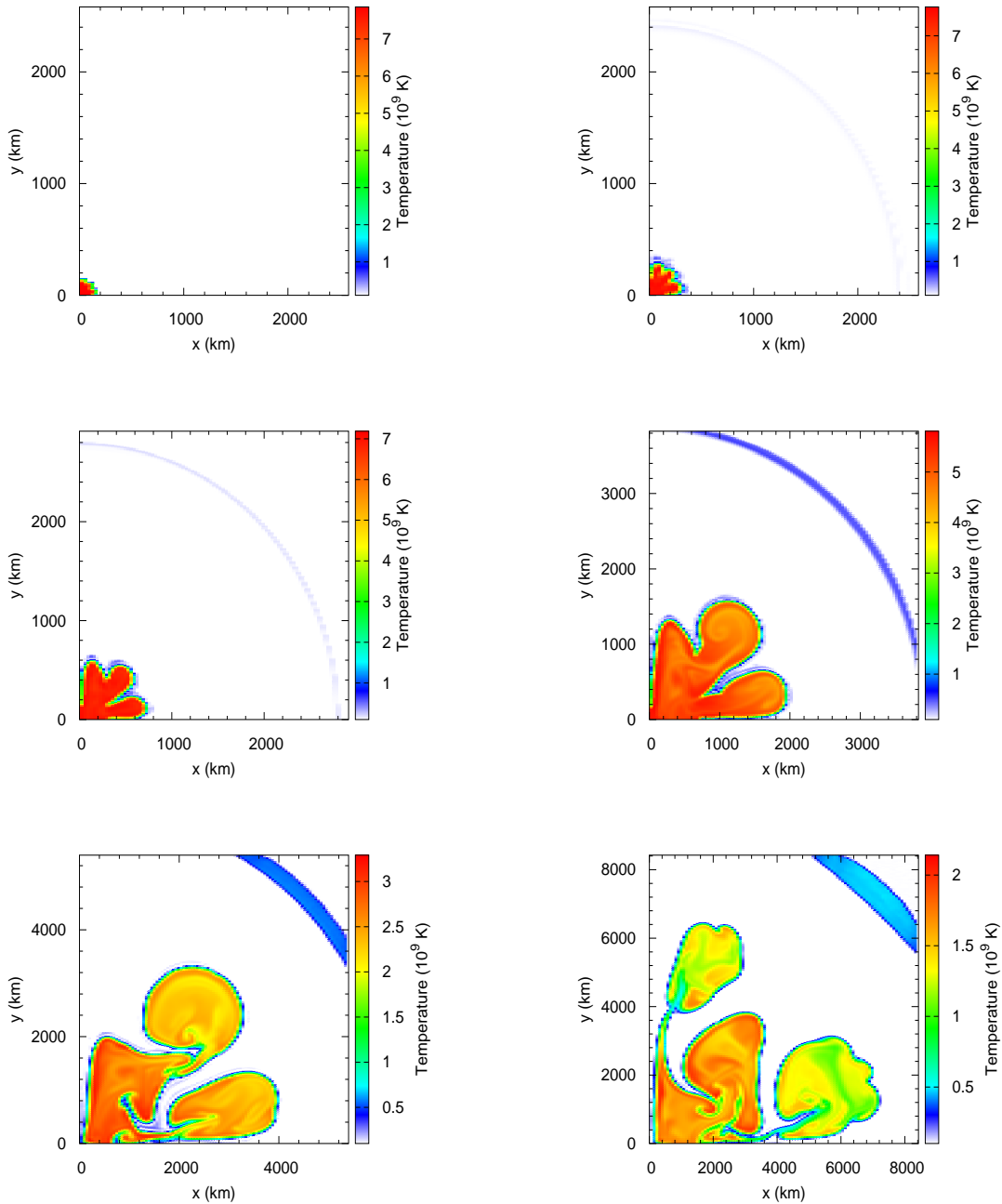


Figure 5. The flame structure and the temperature colour plots of the characteristic model from the beginning to 2.5 s after deflagration has started at an interval of 0.5 s.

flame, the smaller scale “mushroom” shapes emerge as the Rayleigh-Taylor instabilities. This occurs when the lower density ash creates a pressure inversion with the higher density fuel against the gravitational force. Also the inverse “mushroom” shape can be seen at the inner part of the ash, showing the injection of fuel into the ash. The colour map of the temperature further shows instabilities in the smaller length scale inside the ash.

3.4. Isotopic abundance

Unlike normal SNe Ia, the low explosion energy means that the star is not completely disrupted by the nuclear flame. At the beginning, the burnt matter has the largest momentum which can escape from the star. However, during its upward motion, it transferred part of its momentum to the matter of lower density in the outer part of the star. Part of the burnt matter thus

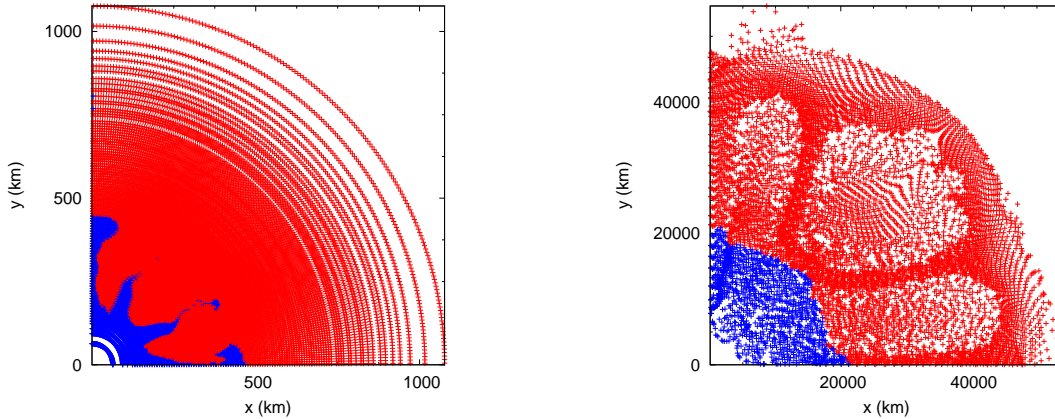


Figure 6. The tracer particle distribution for the particles which can escape (red) and which are gravitationally bounded (blue). The escape criterion is decided by the final energy of the tracer particles. The initial particle distribution (left panel) and the final particle distribution (right panel) are shown for comparison.

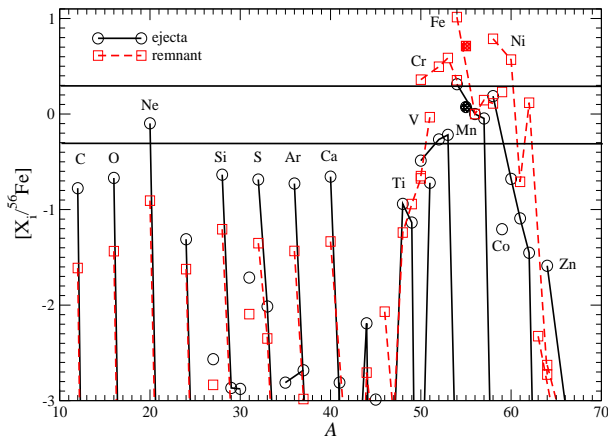


Figure 7. $[X_i/^{56}\text{Fe}]$ against mass number for the characteristic model. The remnant composition and ejecta composition are included.

becomes bounded during this momentum transfer. Instead, the surface matter is expelled. To clarify which part of the star can be ejected, and which part remains bounded in the star, we use the kinematic properties of the tracer particles. For each tracer particle, we obtain its specific kinetic energy $|\vec{v}|^2/2$, and its current gravitational energy $\phi(\vec{r})$, from the end of simulations. We assume that tracer particles can escape when $|\vec{v}|^2/2 + \phi(\vec{r}) > 0$. We notice that the tracer particles satisfying this relation remain unchanged beyond a few seconds after explosion.

In Figure 6 we plot the tracer particles which can escape (red) and which are bounded by its self gravity (blue). We plot the tracer particle distribution according to its initial position (left panel) and its final position (right panel). The initial profile demonstrates which part of the star is being ejected after deflagration. Compared with Figure 5, most of the innermost part of the ash is trapped in the star. Instead, most ma-

terial within 200 km for its original position is trapped, while the particles between 200 – 500 km along the diagonal are partially ejected. The trapped matter in this region is consistent with the flame structure seen in Figure 5. We plot the final position of the ejected particles in the right panel at 10 s after the simulation. The mixing effects can no longer be seen. The ejected matter locates at the outermost part of the star while the trapped matter falls back to form the remnant. The trapped matter is already settled down in the innermost 20000 km. A careful examination at the density of the particles reveals some differences between the ejected ash and ejected fuel. The ejected ash has a lower tracer particle density compared to the ejected fuel. This is related to the thermal expansion of the ash when it arrives the region filled with the cold fuel.

In Figure 7 we plot $[X_i/^{56}\text{Fe}]$ for the characteristic model. Here,

$$[X_i/^{56}\text{Fe}] = \log_{10}[(X_i/X(^{56}\text{Fe})) / (X_i/X(^{56}\text{Fe}))_{\odot}] \quad (1)$$

is the mass fraction ratio to ^{56}Fe of the stable isotopes, relative to the solar ratio. Here, the stable isotopes means that all typical short lifetime radioactive isotopes have decayed. After the post-processing nucleosynthesis yield is obtained, we allows the yield product to decay for $\sim 10^6$ years, such that most radioactive isotopes ^{56}Ni (~ 8 days), ^{57}Ni (~ 60 days), ^{59}Ni (60000 years) have decayed. However, isotopes with a longer half life such as ^{27}Al and ^{60}Fe may not decayed completely. Despite that, these isotopes are not mostly produced in SN Ia. Since the star is partially disrupted, we separate the ejecta and the remnant compositions for comparison. As shown in previous figures, the ejecta are obtained from the tracer particles which have a positive total energy.

The ejecta mostly comes from matter in the surface, where the abundances of O and Ne are abundant. It has

very low masses of intermediate mass elements (IMEs), such as Si, S, Ar and Ca. The lower part iron-peak elements (IPEs), i.e. Ti, V and Cr are also underproduced. On the contrary, upper part of IPEs, i.e. Mn, Fe and Ni are well produced. Zn is underproduced.

In the remnant, it has a similar pattern in O and Ne but is lower by one order of magnitude at 1 – 10% of solar values. The abundances of IMEs in the deflagration ash are also low in the remnant, and they are still underproduced. The IPEs have a more interesting pattern in the remnant. As discussed above, most tracer particles in the inner core failed to escape from the star during the momentum transfer process. The higher Y_e isotopes including ^{54}Fe and ^{58}Ni can be 10 and 8 times higher than the solar ratios. As a result, the lighter part of IPEs, especially the neutron rich ones including ^{51}V , $^{53,54}\text{Cr}$ and ^{55}Mn are higher than the solar ratios. In particular, $^{55}\text{Mn}/^{56}\text{Fe}$ and $^{58}\text{Ni}/^{56}\text{Fe}$ can reach ~ 0.5 and 0.6 respectively. The final remnant WD has a very different composition from standard C+O WD of similar mass ($\sim 0.3 M_\odot$), where the contamination by IMEs and IPEs is significant.

4. MODEL SUMMARY

In this section, we examine the hydrodynamics and nucleosynthesis of our SN Iax models using PTD in C+O WDs and hybrid C+O+Ne WDs.

In Table 1 we tabulate the models computed in this work, and their corresponding exploding energetics and global chemical properties. We name each model according to the model parameters. For example the model 300-137-1-c3-06 means a C+O WD model with a central density $3.00 \times 10^9 \text{ g cm}^{-3}$, CO-rich matter of mass of $1.37 M_\odot$, $1 Z_\odot$, c3-flame and C/O = 0.6 in mass fraction, i.e. $X(^{12}\text{C}) = 0.366$, $X(^{16}\text{O}) = 0.609$ and $X(^{22}\text{Ne}) = 0.025$. For hybrid C+O+Ne WDs, the second entry is the mass of CO-rich matter before we mix the composition by hand. The last entry does not apply to hybrid C+O+Ne WDs.

5. PURE TURBULENT DEFLAGRATION IN C+O WHITE DWARFS

In this section we study in details the nucleosynthesis yields of C+O WDs which explode as SNe Iax. For the C+O WDs with the initial central density $\rho_{c,\text{ini}}$ and metallicity Z as the model parameters, we put in the initial centered or off-center flame. We follow the flame propagation and the expansion of the star until the star develops into homologous expansion. After that, we use the thermodynamical histories of the tracer particles to calculate the post-process nucleosynthesis. In Table 3, 4 and 5 we tabulate the nucleosynthesis yield and the radioactive isotopes in the ejecta.

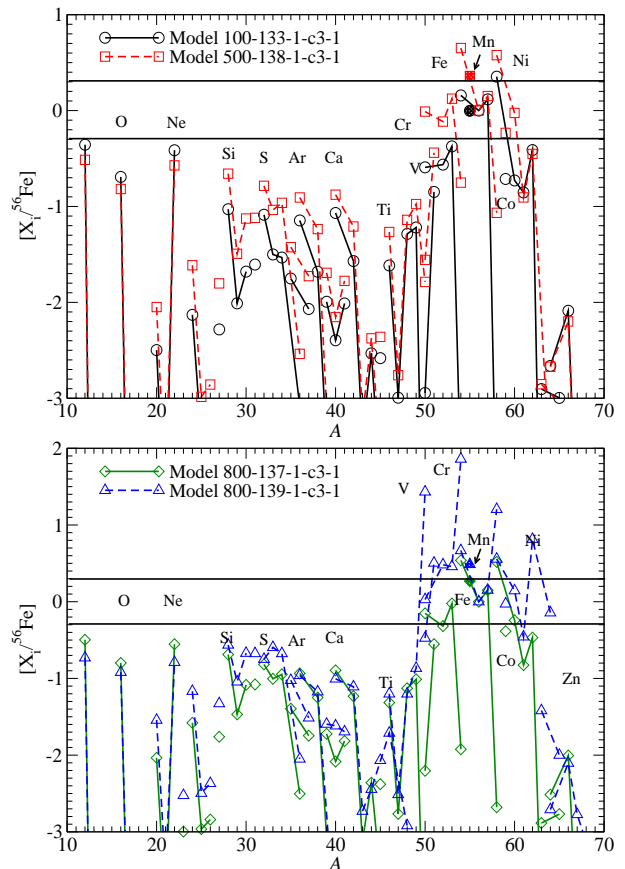


Figure 8. $[X_i/^{56}\text{Fe}]$ against mass number for the ejecta of C+O WD models for Models 100-133-1-c3-1 ($\rho_c = 1 \times 10^9 \text{ g cm}^{-3}$) and 500-138-1-c3-1 ($\rho_c = 5 \times 10^9 \text{ g cm}^{-3}$) in the top panel, and Models 300-137-1-c3-1 ($\rho_c = 3 \times 10^9 \text{ g cm}^{-3}$) and 800-138-1-c3-1 ($\rho_c = 8 \times 10^9 \text{ g cm}^{-3}$) in the bottom panel. All models assume no O+Ne-rich matter, $X(^{22}\text{Ne}) = 0.025$, c3 initial flame and C/O ratio = 1.

5.1. Ejecta of C+O White Dwarf

5.1.1. Dependence on Central Density of White Dwarf

In Figure 8 we plot the abundance ratios $[X/^{56}\text{Fe}]$ in the ejecta of Models 100-133-1-c3-1 ($\rho_c = 10^9 \text{ g cm}^{-3}$), 300-137-1-c3-1 ($\rho_c = 3 \times 10^9 \text{ g cm}^{-3}$), 500-137-1-c3-1 ($\rho_c = 5 \times 10^9 \text{ g cm}^{-3}$) and 800-137-1-c3-1 ($\rho_c = 8 \times 10^9 \text{ g cm}^{-3}$). These are the models based on C+O WDs with different ρ_c . In the top panel we plot the abundance patterns for Models 100-133-1-c3-1 and 500-133-1-c3-1, while in the bottom panel the other two. More IMEs appear in the ejecta of higher ρ_c except for the very high $\rho_c = 8 \times 10^9 \text{ g cm}^{-3}$. At low density ($1 - 5 \times 10^9 \text{ g cm}^{-3}$) the IPEs are comparable to the solar ratios with larger $[X/\text{Fe}]$ for higher ρ_c . Isotope ratios including $^{50,52,53}\text{Cr}$, ^{54}Fe , ^{55}Mn and ^{58}Ni are larger for higher ρ_c . At high ρ_c , the increase in ^{54}Fe , ^{55}Mn and ^{58}Ni levels off. Instead, neutron-rich isotopes including ^{51}V , ^{54}Cr , ^{60}Fe and ^{62}Ni become severely overproduced relative to the solar ratio.

Table 1. The model parameters of the models studied in this work. "Type" corresponds to the classification of the WD being a carbon-oxygen (C+O) WD or a hybrid carbon-oxygen-neon (C+O+Ne) WD. M , M_{CO} , M_{ONe} , M_{Ni} , M_{ej} , M_{rem} are the mass of the initial WD, the C+O part, the O+Ne part, the total ^{56}Ni produced in the ejecta, the ejecta mass and the remnant mass in units of M_{\odot} . R and R_{core} are the radius of the initial WD and the core (if applicable), in units of km. E_{tot} and E_{nuc} are the final total energy and the nuclear energy produced by the deflagration in units of 10^{50} erg. Z is the metallicity in units of Z_{\odot} . ρ_c and ρ_{core} are the initial central density and core-envelope interface density (if applicable) in units of 10^9 g cm^{-3} . Notation "flame" corresponds to the initial geometry of the flame, including c3 (three-"finger" structure) and the b1 (one bubble) structure. "Others" includes setting specific to that corresponding type of WD.

Type	Model	ρ_c	Z	M	M_{CO}	M_{ONe}	flame	R	E_{tot}	E_{nuc}	M_{ej}	M_{rem}	M_{Ni}	others
CO WD	050-130-1-c3-1	0.50	1	1.30	1.30	N/A	c3	3070	-1.61	2.36	0.00	1.30	0.00	C/O = 1
CO WD	100-133-1-c3-1	1.00	1	1.33	1.33	N/A	c3	2580	2.23	6.71	0.92	0.41	0.23	C/O = 1
CO WD	200-135-1-c3-1	2.00	1	1.35	1.35	N/A	c3	2170	3.69	8.52	1.18	0.17	0.24	C/O = 1
CO WD	300-137-1-c3-1	3.00	1	1.37	1.37	N/A	c3	1950	4.54	9.69	1.26	0.11	0.34	C/O = 1
CO WD	500-138-1-c3-1	5.00	1	1.38	1.38	N/A	c3	1710	5.13	10.5	1.29	0.09	0.32	C/O = 1
CO WD	550-138-1-c3-1	5.50	1	1.38	1.38	N/A	c3	1670	5.81	11.0	1.30	0.08	0.31	C/O = 1
CO WD	600-138-1-c3-1	6.00	1	1.38	1.38	N/A	c3	1620	6.03	11.2	1.31	0.07	0.30	C/O = 1
CO WD	750-139-1-c3-1	7.50	1	1.39	1.39	N/A	c3	1540	6.25	11.5	1.33	0.06	0.32	C/O = 1
CO WD	800-139-1-c3-1	8.00	1	1.39	1.39	N/A	c3	1500	7.51	12.7	1.34	0.05	0.31	C/O = 1
CO WD	900-140-1-c3-1	9.00	1	1.40	1.40	N/A	c3	1460	7.81	13.1	1.36	0.04	0.34	C/O = 1
CO WD	100-133-1-b1-1	1.00	1	1.33	1.33	N/A	b1	2580	2.99	7.47	1.03	0.30	0.23	C/O = 1
CO WD	300-137-1-b1-1	3.00	1	1.37	1.37	N/A	b1	1950	4.82	9.97	1.19	0.19	0.26	C/O = 1
CO WD	500-138-1-b1-1	5.00	1	1.38	1.38	N/A	b1	1710	6.50	11.9	1.20	0.18	0.30	C/O = 1
CO WD	550-138-1-b1-1	5.50	1	1.38	1.38	N/A	b1	1670	6.50	11.9	1.20	0.18	0.29	C/O = 1
CONe WD	100-043-1-c3	1.00	1	1.33	0.43	0.90	c3	2580	1.89	6.30	0.96	0.37	0.18	
CONe WD	200-045-1-c3	2.00	1	1.35	0.45	0.90	c3	2160	2.93	7.74	1.11	0.24	0.24	
CONe WD	300-047-1-c3	3.00	1	1.37	0.47	0.90	c3	1950	4.54	9.69	1.15	0.22	0.28	
CONe WD	500-048-1-c3	5.00	1	1.38	0.48	0.90	c3	1710	5.13	10.5	1.26	0.12	0.36	
CONe WD	550-048-1-c3	5.50	1	1.38	0.48	0.90	c3	1670	4.42	9.59	1.26	0.12	0.33	
CONe WD	750-049-1-c3	7.50	1	1.39	0.49	0.90	c3	1540	5.39	10.6	1.29	0.10	0.35	
CONe WD	900-050-1-c3	9.00	1	1.40	0.50	0.90	c3	1460	5.92	11.1	1.33	0.07	0.36	
CONe WD	100-043-1-b1	1.00	1	1.33	0.43	0.90	b1	2580	2.69	7.15	0.97	0.36	0.20	
CONe WD	200-045-1-b1	1.00	1	1.35	0.45	0.90	b1	2160	3.78	8.68	1.10	0.25	0.23	
CONe WD	300-047-1-b1	3.00	1	1.37	0.47	0.90	b1	1950	4.66	9.78	1.12	0.25	0.31	
CONe WD	500-048-1-b1	5.00	1	1.38	0.48	0.90	b1	1710	5.13	10.5	1.17	0.21	0.32	
CONe WD	550-048-1-b1	5.50	1	1.38	0.48	0.90	b1	1670	5.81	11.0	1.18	0.20	0.32	
CONe WD	750-049-1-b1	7.50	1	1.39	0.49	0.90	b1	1540	5.72	11.3	1.21	0.18	0.32	
CONe WD	900-050-1-b1	9.00	1	1.40	0.50	0.90	b1	1460	7.81	13.1	1.30	0.10	0.35	

5.1.2. Dependence on Initial Flame Structure

We examine the effects of initial flame structure to the nucleosynthesis yield for C+O WD models. In Figure 9 we plot $[X/^{56}\text{Fe}]$ in the ejecta for Models 300-137-1-c3-1 (c3 flame) and 300-137-1-b1-1 (b1 flame). The two WD models share the same configuration but with different initial flame geometry.

The differences between the two models are small. IMEs show systematic downward shifts when the initial flame moves from center to off-center. This suggests that the mass of ^{56}Fe as the denominator changes instead of the change in individual isotope yields. Similar

changes can be observed for the IPEs too. On the contrary, the off-center burning facilitates the production of IPEs. It is because the IPEs produced in the off-center flame can be more readily ejected than those produced at the center.

However we remark that the effects in three-dimensional model can be larger, as shown in Röpke et al. (2006a); Seitenzahl et al. (2013); Fink et al. (2014). Three-dimensional simulations can accommodate a more complex flame structure and hence more diversified distributions in the ejecta abundance.

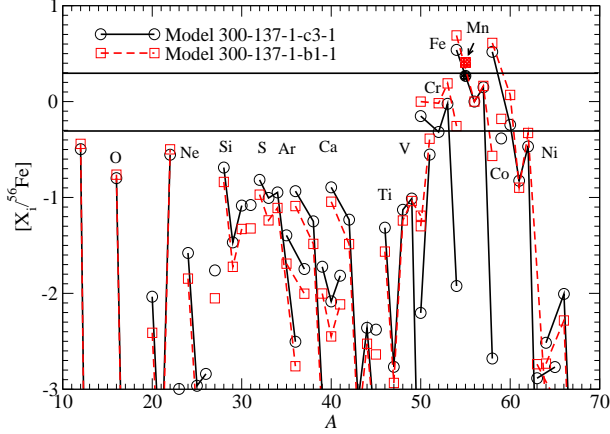


Figure 9. Scaled mass fraction $[X_i/^{56}\text{Fe}]$ against mass number for the ejecta of C+O WD models for Models 300-137-1-c3-1 (*c3* flame) and 300-137-1-b1-1 (*b1* flame). All models assume $\rho_c = 3 \times 10^9 \text{ g cm}^{-3}$, no hybrid O+Ne+Mg-rich matter, $X(^{22}\text{Ne}) = 0.025$, and C/O ratio = 1.

5.1.3. Dependence on C/O ratio

We examine the effects of the initial C/O ratio on the nucleosynthesis yields of C+O WD models. The uncertainty in the C/O ratio mainly stems from the uncertainties in the $^{12}\text{C}(\alpha, \gamma)^{16}\text{O}$ rate and the convective overshooting during He burning in the progenitor.

In Figure 10 we plot $[X/^{56}\text{Fe}]$ in the ejecta for Models 300-137-1-c3-06 ($C/O = 0.6$) and 300-137-1-c3-03 ($C/O = 0.3$). The two WD models share the same configuration but with a different C/O ratio.

The effects of C/O ratio are much smaller than the previous two parameters. We find almost no change in IPEs and small enhancements in the IMEs for the low C/O ratio. This is because slower flame for the low C/O ratio produces lower energy, thus the amount of matter experiencing incomplete burning increases.

5.1.4. Dependence on turbulent flame speed

We examine the effects of turbulent flame speed on the nucleosynthesis yield of the C+O WD models. In Figure 11 we plot the final abundance pattern of the ejecta for Models 300-137-1-c3-1-f05 and 300-137-1-c3-1-f025. The two WD models share the same configuration but with different asymptotic turbulent flame speed (at 50 % and 25% of the standard prescription). That means, we alter C_A in the turbulent flame speed formula

$$v_{\text{flame}} = v_{\text{lam}}(\rho) \sqrt{1 + C_A(v'/v_{\text{lam}})^2}, \quad (2)$$

where $v_{\text{lam}}(\rho)$ and v' are the laminar flame propagation speed and the velocity fluctuations due to turbulent motion. We can see that at $v' \rightarrow 0$, $v_{\text{flame}} = v_{\text{lam}}(\rho)$. This means that the flame propagates like a laminar wave when the flow is not turbulent. Otherwise, when

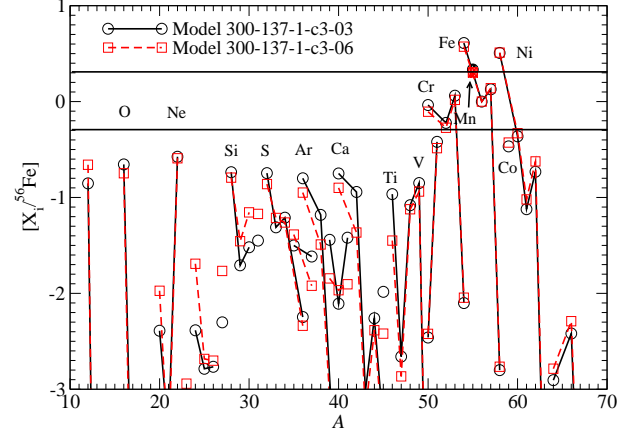


Figure 10. $[X_i/^{56}\text{Fe}]$ against mass number for the ejecta of C+O WD models for Models 300-137-1-c3-06 ($C/O = 0.6$) and 300-137-1-c3-03 ($C/O = 0.3$). All models assume $\rho_c = 3 \times 10^9 \text{ g cm}^{-3}$, no O+Ne+Mg-rich matter, $X(^{22}\text{Ne}) = 0.025$ and *c3* initial flame.

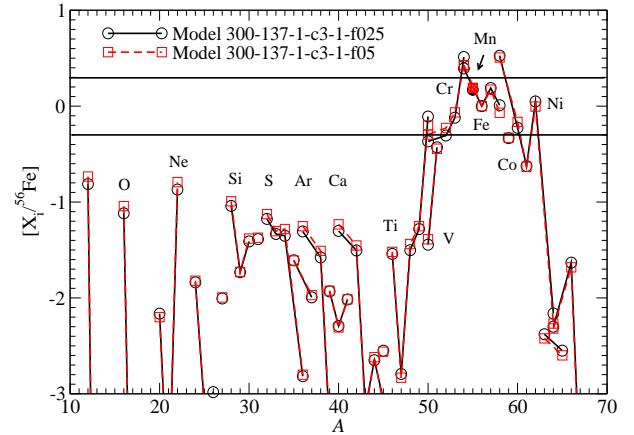


Figure 11. $[X_i/^{56}\text{Fe}]$ against mass number for the ejecta for Models 300-137-1-c3-1-f05 ($v_{\text{flame}} = 0.5 v_{\text{flame},0}$) and 300-137-1-c3-1-f025 ($v_{\text{flame}} = 0.25 v_{\text{flame},0}$). All models assume $\rho_c = 3 \times 10^9 \text{ g cm}^{-3}$, no hybrid O+Ne+Mg layer, $X(^{22}\text{Ne}) = 0.025$, *c3* initial flame and C/O ratio = 1.

$v' \gg v_{\text{lam}}$, $v_{\text{flame}} \rightarrow \sqrt{C_A} v'$. This means that the flame burns with a speed following the turbulent motion.

We remark that the connection between turbulent velocity fluctuations v' and the corresponding flame velocity is not yet well constrained because the corresponding WD condition and environment cannot be reproduced in any laboratory. It is unclear how the flame speed scales with v' in the turbulent regime, where in a WD the Reynolds number can be as high as 10^{14} . Formula based on theoretical arguments can be found in, e.g., Hicks (2015).

In contrast to our previous works, the flame velocity has almost no effect on the chemical yields of our models. There are very minor differences in IMEs.

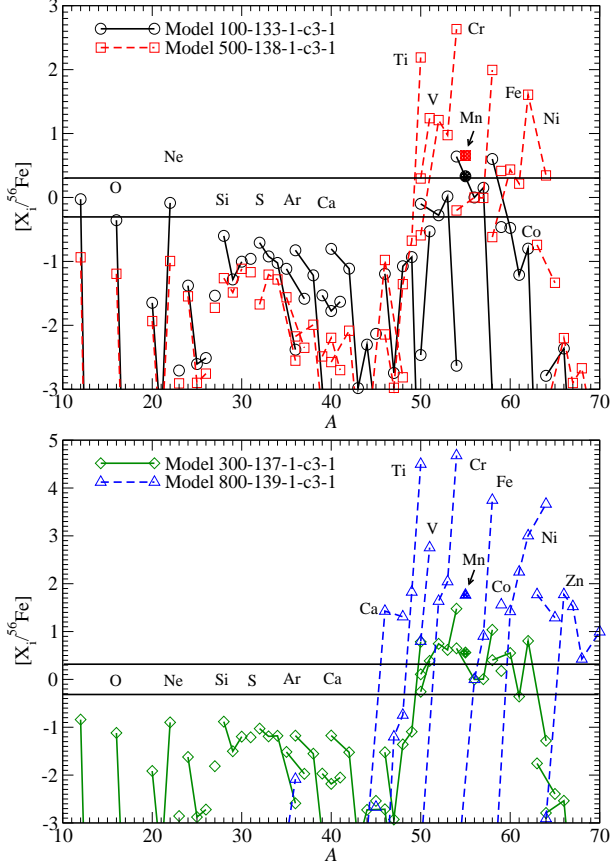


Figure 12. $[X_i/^{56}\text{Fe}]$ against mass number for remnants of C+O WD models for Models 100-130-1-c3-1 ($\rho_c = 1 \times 10^9 \text{ g cm}^{-3}$) and 500-138-1-c3-1 ($\rho_c = 5 \times 10^9 \text{ g cm}^{-3}$) in the top panel, 300-137-1-c3-1 ($\rho_c = 3 \times 10^9 \text{ g cm}^{-3}$) and 800-139-1-c3-1 ($\rho_c = 8 \times 10^9 \text{ g cm}^{-3}$) in the bottom panel. All models assume no hybrid O+Ne+Mg-rich matter $X(^{22}\text{Ne}) = 0.025$, c3 initial flame and C/O ratio = 1.

5.2. Remnant of PTD in C+O White Dwarf

5.2.1. Dependence on Central Density

In Figure 12 we study the effects of initial ρ_c of the WD on the nucleosynthesis yields in the bounded remnants WDs. Similar to the characteristic model, the bounded remnant is defined by the tracer particles which have a negative total energy at the end of simulations (10 s after the flame starts). The effects of ρ_c are consistent with our earlier work (Leung & Nomoto 2018).

In the top panel, we plot the Models 100-000-1-c3-1 and Model 500-000-1-c3-1 of the remnant part and in the bottom panel the other two models. Similar to the ejecta, with increasing ρ_c , masses of IMEs decrease. For the very high ρ_c , the remnant does not contain any C+O+Ne-rich matter or IMEs. This is because those matter, which are synthesized at the outer region of a lower density (10^8 g cm^{-3} or below), are also ejected without fallback by the stronger deflagration. In all

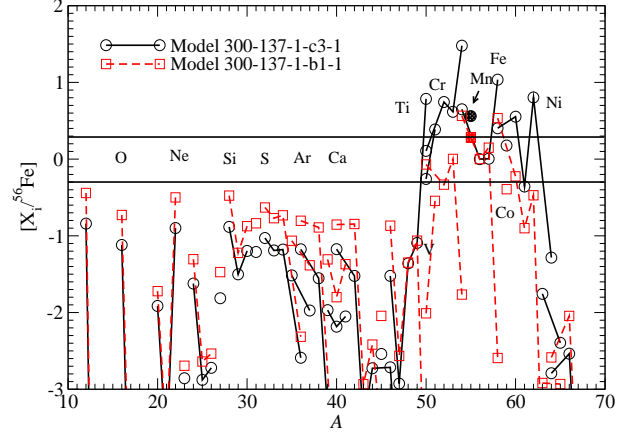


Figure 13. $[X_i/^{56}\text{Fe}]$ against mass number for the bounded remnant of C+O WD models for Models 300-137-1-c3-1 (c3 flame) and 300-137-1-b1-1 (b1 flame). All models assume $\rho_c = 3 \times 10^9 \text{ g cm}^{-3}$, no hybrid O+Ne+Mg-rich matter, $X(^{22}\text{Ne}) = 0.025$ and C/O ratio = 1.

models, IMEs are always underproduced. The IMEs decrease with increasing ρ_c because more matter can be burnt at a lower density before the flame quenches.

The IPEs show more interesting features. Isotopes with a high Y_e gradually decrease in its abundance when ρ_c increases. Neutron-rich isotopes are robustly over-produced in the remnant. At a central density $3 \times 10^9 \text{ g cm}^{-3}$ isotopes like ^{54}Cr and ^{58}Fe are over-produced, especially for Models 500-138-1-c3-1 and 800-139-1-c3-1. At a higher ρ_c , IPEs from Ca to Zn are found in the remnant. Their abundances can exceed the solar values by a factor of 10^{2-5} in Model 800-139-1-c3-1.

We remark that in interpreting the remnant composition, it is also useful to examine the element abundances instead of isotope abundances because the spectra from WD remnants do not distinguish isotopes. We also show the element distribution in Section 7.

5.2.2. Dependence on Initial Flame Structure

In Figure 13 we study the effects of initial flame on the remnant nucleosynthesis pattern. We plot the abundance pattern of Models 300-137-1-c3-1 and 300-137-1-b1-1. They differ only by the position of the initial flame (center versus. off-center). Consistent with the ejecta composition, the remnant consists of high abundances of IMEs when the flame is off-center. When the initial flame is farther from the center, the over-production of some neutron-rich isotopes is less severe. This can be seen as a systematic drop in isotopes like $^{52-54}\text{Cr}$, ^{55}Mn , ^{58}Fe and $^{60-64}\text{Ni}$. Higher Y_e isotopes of Fe and Ni remain similar. These features are in general consistent with the picture that the off-center flame can push

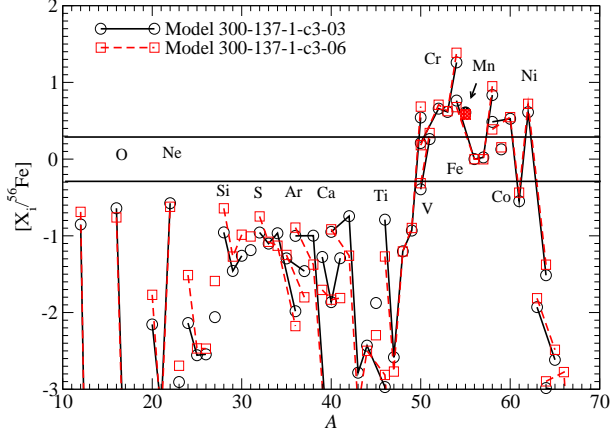


Figure 14. $[X_i/^{56}\text{Fe}]$ against mass number for the bounded remnant of C+O WD models for Models 300-137-1-c3-06 ($C/O = 0.6$) and 300-137-1-c3-03 ($C/O = 0.3$). All models assume $\rho_c = 3 \times 10^9 \text{ g cm}^{-3}$, no hybrid O+Ne+Mg-rich matter, $X(^{22}\text{Ne}) = 0.025$ and c3 initial flame.

matter more easily outward as the momentum transport does not necessarily start in the center.

5.2.3. Dependence on C/O ratio

In Figure 14 we plot the abundance pattern for the remnants of Models 300-137-1-c3-06 and 300-137-1-c3-03. The two models differ by the C/O ratio, which changes not only the initial chemical composition, but also the energy production by the deflagration and the laminar flame speed. The differences between the two models are slightly stronger than the ejecta. Enhanced isotopes of IMEs such as ^{38}Ar and ^{42}Ca can be observed. The IPEs are shifted upward systematically when C/O ratio decreases, again suggesting the changes of ^{56}Fe .

5.2.4. Dependence turbulent flame speed

At last in Figure 15 we compare the effects of asymptotic turbulent flame speed on the remnant composition for Models 300-137-1-c3-1-f025 and 300-137-1-c3-1-f05. Similar to the ejecta, the difference of flame speed we chose does not affect the abundance pattern in an observable level. A systematic decrease for most isotopes can be observed when v_{flame} increases, suggesting that the flame produces more ^{56}Fe as a result. When a slower flame model is used, a systematic enhancement of C+O-rich matter and IMEs can be found in the remnant. The abundances of neutron-rich IPEs increase when the flame speed increases too. Meanwhile, there is no significant enhancement for IPEs with a higher Y_e .

6. HYBRID C+O+NE WD

In this section we study how the model parameters affect the explosive nucleosynthesis of the hybrid

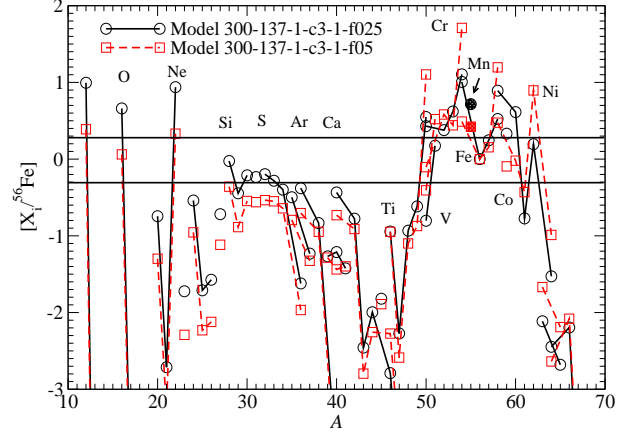


Figure 15. $[X_i/^{56}\text{Fe}]$ against mass number for the bounded remnant of C+O WD models for Models 300-137-1-c3-1-f025 ($v_{\text{flame}} = 0.25 v_{\text{flame},0}$) and 300-137-1-c3-1-f05 ($v_{\text{flame}} = 0.5 v_{\text{flame},0}$). All models assume $\rho_c = 3 \times 10^9 \text{ g cm}^{-3}$, no hybrid O+Ne+Mg-rich matter, $X(^{22}\text{Ne}) = 0.025$, c3 initial flame and C/O ratio = 1.

C+O+Ne WD. In Table 6, 7 and 8 we tabulate the nucleosynthesis yields and the masses of radioactive isotopes in the ejecta.

6.1. Ejecta of Hybrid C+O+Ne WD

6.1.1. Dependence on Central Density

In Figure 16 we plot $[X_i/^{56}\text{Fe}]$ in the ejecta of the hybrid C+O+Ne WDs for Models 100-043-1-c3, 300-047-1-c3, 500-048-1-c3 and 700-049-1-c3.

The abundance pattern of the ejecta is similar to the typical SN Ia. (1) IMEs are underproduced. (2) The V, Cr, Mn and Co isotopes are much higher in the higher central density models than the lower density models. (3) On the contrary, Fe and Ni isotopes are not sensitive to the central density except that ^{54}Fe and ^{58}Ni are higher for the higher central density. (4) Only in extreme cases such as Model 750-049-1-c3 we observe the severe overproduction of the neutron-rich isotopes ^{50}Ti , ^{54}Cr , ^{58}Fe and ^{62}Ni . (5) A growth of Mn with increasing central density is still seen but it saturates at a value $[\text{Mn}/\text{Fe}] \sim 2$, while $[\text{Co}/\text{Fe}]$ becomes compatible with the solar value.

The overall trend is similar to C+O WD models. The C+O+Ne composition only provides a lower energy release due to the lower abundance of ^{12}C and a higher abundance of ^{20}Ne . The C+O+Ne composition also makes the flame propagation slower. In general the turbulent flame dominates the flame propagation, which is independent on the composition. But the composition affects the turbulent flame indirectly by its energy feedback, which changes the turbulent motion inside the

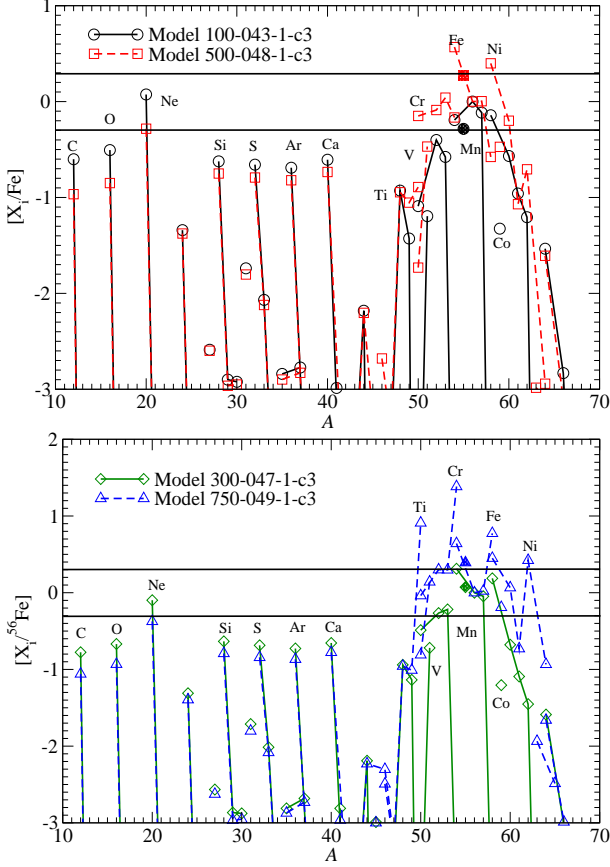


Figure 16. $[X_i/^{56}\text{Fe}]$ against mass number for the ejecta of C+O WD models for Models 100-043-1-c3 ($\rho_c = 1.0 \times 10^9 \text{ g cm}^{-3}$) and 500-048-1-c3 ($\rho_c = 5.0 \times 10^9 \text{ g cm}^{-3}$) in the top panel, Models 300-047-1-c3 ($\rho_c = 3.0 \times 10^9 \text{ g cm}^{-3}$) and 750-049-1-c3 ($\rho_c = 7.5 \times 10^9 \text{ g cm}^{-3}$) in the bottom panel. All models assume $X(^{22}\text{Ne}) = 0.025$ and c3 initial flame.

star, and hence the production and decay of turbulent motion.

In general, the CO-deflagration does not differ much from CONe-deflagration at high density because in both cases, matter is burnt into NSE. By comparing Figure 16 with Figure 8, the overall patterns suggest that, indeed, the property of CO-deflagration and CONe-deflagration does not differ much except for the minor details, such as the minor isotopes in IMEs and lower mass IPEs. But we remind that a hybrid C+O+Ne WD, takes a longer time for the deflagration wave to spread and burn to release the necessary energy for the expansion. This also means the momentum transport from the hot ash to the cold fuel is slower.

6.1.2. Dependence on Initial Flame Structure

We examine the effects of initial flame structure on the nucleosynthesis yield for the hybrid C+O+Ne WDs. In Figure 17 we plot $[X_i/^{56}\text{Fe}]$ of the ejecta for Models 300-047-1-c3 and 300-047-1-b1. The two WD models

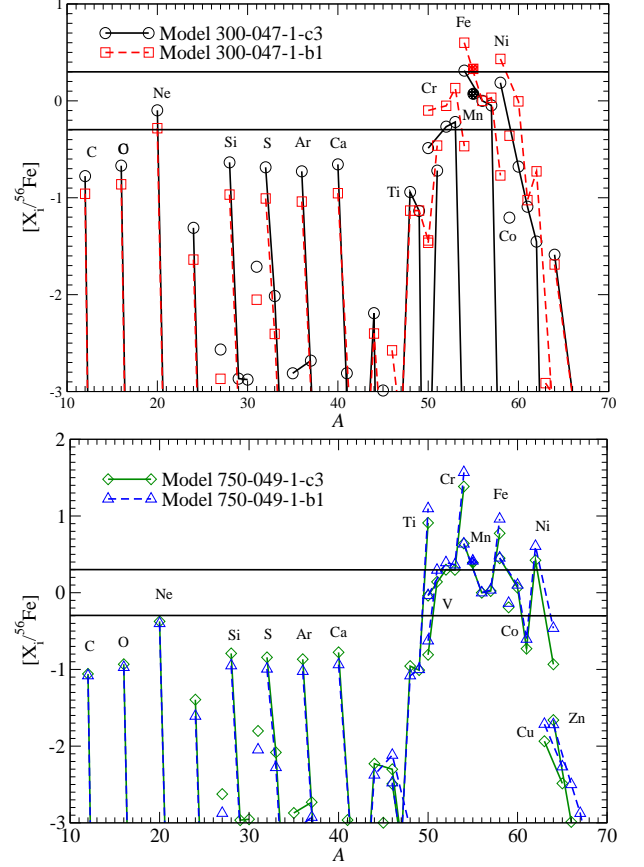


Figure 17. (top panel) $[X_i/^{56}\text{Fe}]$ against mass number for the ejecta in hybrid C+O+Ne WD models for 300-047-1-c3 (c3 flame) and 300-047-1-b1 (b1 flame). (bottom panel) Same as the upper panel, but for Models 750-049-1-c3 and 750-049-1-b1. All models assume $X(^{22}\text{Ne}) = 0.025$ and c3 initial flame.

share the same configuration but with different initial flame geometry (centered flame c3 vs. off-center flame b1).

As a demonstration we compare the final nucleosynthesis yields of the ejecta in Models 300-047-1-c3 and 300-047-1-b1 in the upper panel and Models 750-049-1-c3 and 750-049-1-b1 in the lower panel. The two models differ by the initial flame where one is the central c3 flame and the other is off-centered b1 flame. The ejecta composition is very similar in both cases in the light elements of O, Ne, and IMEs such as Si, S, Ar and Ca. Off-center flame gives a slightly lower or a comparable amount of C, O, Ne and IMEs. The difference of the flame mostly affects IPEs. In the lower density models, the off-center flame tends to produce more Cr, Fe, Mn and Ni with very significant overproduction. Strong enhancement of ^{59}Co for the b1-flame model can be seen. This is because the IPEs, which are produced in the core region, can be transported more easily by the flame bub-

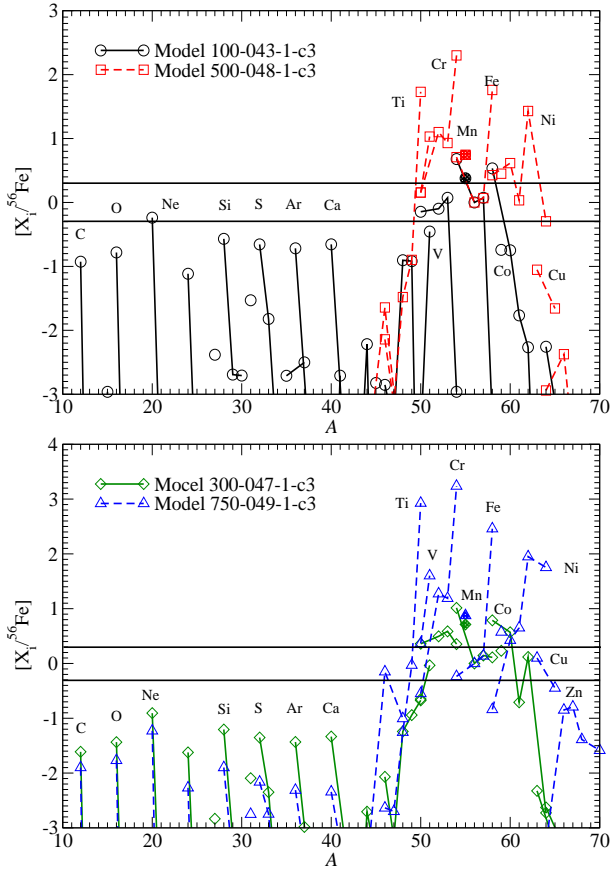


Figure 18. $[X_i/^{56}\text{Fe}]$ against mass number for the remnants of hybrid C+O+Ne WD models for Models 100-043-1-c3 ($\rho_c = 1.0 \times 10^9 \text{ g cm}^{-3}$) and 500-048-1-c3 ($\rho_c = 5.0 \times 10^9 \text{ g cm}^{-3}$) in the top panel, Models 300-047-1-c3 ($\rho_c = 3.0 \times 10^9 \text{ g cm}^{-3}$) and 750-049-1-c3 ($\rho_c = 7.5 \times 10^9 \text{ g cm}^{-3}$) in the bottom panel. All models assume $X(^{22}\text{Ne}) = 0.025$ and c3 initial flame.

ble which flows with buoyancy. On the other hand, IPES produced in the central region tend to fallback when they transport their momentum to outer fluid elements. In the high-density models, not much difference in the pattern can be found. This is because the propagation becomes so rapid and energetic that the flame burn similarly and ejects most of the WD.

6.2. Remnant of Hybrid C+O+Ne WD

6.2.1. Dependence on Central Density

In Figure 18 we plot the abundance patterns of the bound remnants in Models 100-043-1-c3, 300-047-1-c3, 500-048-1-c3 and 750-049-1-c3. This series of models studies the effects of the central density of the WD on the chemical composition of the remnant.

From both panels it shows that the initial central density strongly influences the IPES in the remnant. A higher central density leads to a stronger enhancement of neutron-rich isotopes like ^{50}Ti , ^{54}Cr , ^{58}Fe and ^{62}Ni .

Their ratios to ^{56}Fe can be from 10 to 10000 times of the solar ratio. The trend can be seen already in the C+O WDs. Isotopes, with a $Y_e \approx 0.5$, for example, ^{46}Ti , ^{50}Cr , ^{54}Fe and ^{58}Ni , share similar ratios among all models. This is consistent with our previous results that matter with a higher density has a faster electron capture rate, which strongly favours the production of neutron-rich isotopes.

The general abundances of the IMEs (Si, S, Ar, Ca) drop when the progenitor mass increases. It is because as the mass increases, the star becomes more compact, and the density drop in the outer part becomes steeper. Thus there is a lower mass of matter with a low density ($\sim 10^7 \text{ g cm}^{-3}$). One exception is in Model 500-048-1-c3. In that model no C+O+Ne-rich matter and no IMEs can be found. This feature is comparable with Model 800-139-1-c3. The non-monotonic trend suggests that the fallback event is sensitive to how outer matter is ejected. However, we remind that even the IME abundances are higher in Model 800-049-1-c3, it is only about a few % of the solar values.

Despite that some isotopes are extremely over-produced compared to the solar ratio, we remind that their corresponding masses as a part of the element can still be smaller or only comparable with the major isotopes of their corresponding elements. In particular, in spectrography, the atomic lines are sensitive to the elements, but not individual isotopes.

6.2.2. Dependence on Initial Flame Structure

In Figure 19 we compare the chemical composition of the remnant in Models 300-047-1-c3 and 300-047-1-b1 in the upper panel and Models 750-049-1-c3 and 750-049-1-b1 in the lower panel. The two models differ by the initial flame.

In the low density models, the remnant composition is characterized by a significant overproduction of IPES. Larger amounts of C+O+Ne-rich matter and IMEs are observed, again suggesting that an off-center flame help to eject matter more easily due to weaker gravitational attraction and less matter on top of burnt matter. On the other hand, a farther flame from the center produces ash which has experienced less electron capture before the ash cools down. The difference can be seen by the abundance of neutron-rich isotopes ^{54}Cr , ^{58}Fe and ^{59}Co , ^{62}Ni . Apart from that the pattern of IPES is similar.

Then we also compare the abundance yields using different initial flame for the high density models. The abundance pattern is less sensitive to the initial flame structures. C+O+Ne-rich matter and IMEs are higher in the off-center flame model (750-049-1-b1) while there

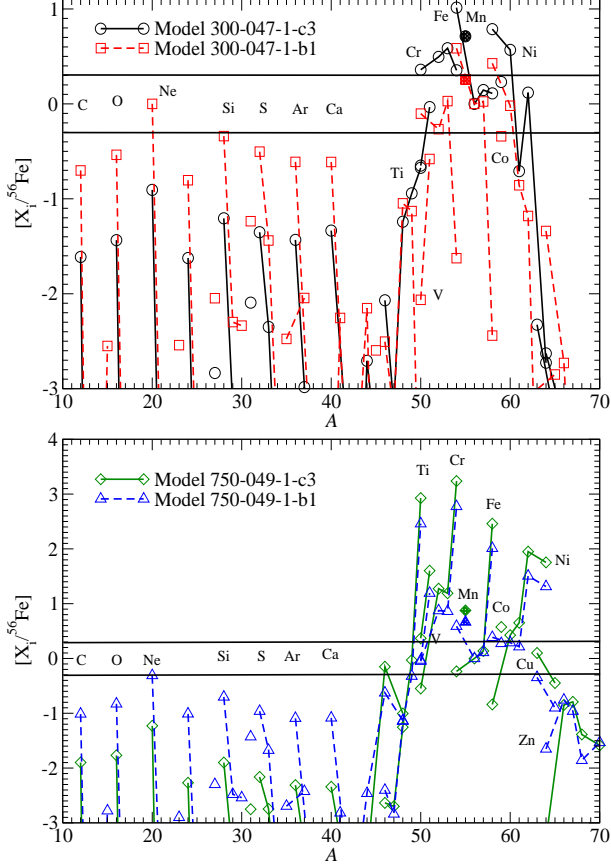


Figure 19. (top panel) $[X_i/^{56}\text{Fe}]$ against mass number for the remnants of hybrid C+O+Ne WD models for Models 300-047-1-c3 (c3 flame) and 300-047-1-b1 (b1 flame). (bottom panel) Similar to the top panel but for 750-049-1-c3 (c3 flame) and 750-049-1-b1 (b1 flame). All models assume $X(^{22}\text{Ne}) = 0.025$ and C/O ratio = 1.

is a higher abundance of IPEs in the centered flame model (750-049-1-c3).

7. DISCUSSION

7.1. Ejecta and its Observable

7.1.1. Ejecta mass - Ejecta energy relation

In observing SNe Iax, the parameter space ($M_{\text{ej}}, E_{\text{ej}}$), i.e. the pair of ejecta mass and the ejecta energy, is important owing to the presence of bounded remnant.

To derive this relation, we collect the final kinetic energy of the ejecta, together with their total mass. In Figure 20 we plot the ejecta mass against the WD final energy for the models presented in this work. We can see a clear monotonic trend where the higher final energy corresponds to a higher ejecta mass. A quasi-linear relation can be seen for $E_{\text{ej}} < 6 \times 10^{50}$ erg. For E_{ej} greater than that, the data approaches the asymptotic value of $\sim 1.4 M_{\odot}$ and levels off.

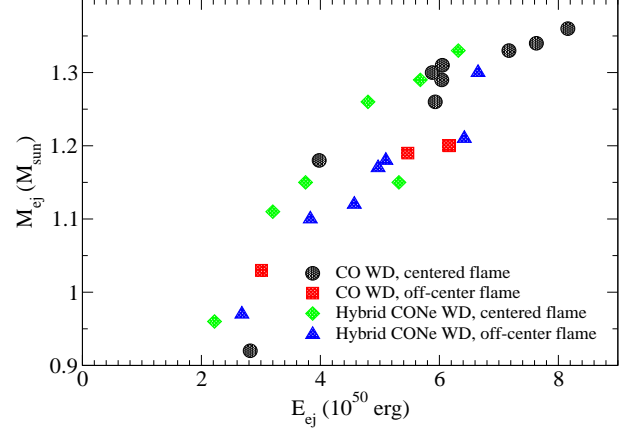


Figure 20. Ejecta mass against final WD ejecta energy for all models in this work.

We further fit the data points with a linear relation at low E_{ej} . We observe a linear relation for E_{ej} between $2 - 6 \times 10^{50}$ erg as $M_{\text{ej}} = 0.9 + 0.1E_{\text{ej}}$ with a chi-square about 0.28. However we expect that the linear relation will break down in the low E_{ej} limit as it corresponds to the limit where the ejecta has no energy, meaning that no ejecta exists. In that case, the relation should fall steeply towards the origin.

7.1.2. Ejecta mass - ^{56}Ni Mass Relation

The ejecta mass - ^{56}Ni mass relation provides a test on how explosion strength is connected to the light curve feature. In general the ejecta mass is related to the width and the ^{56}Ni mass are related to the width and peak luminosity of the light curve respectively. We plot in Figure 21 the ejecta mass against ^{56}Ni for all models we presented in this work. Each group of SN Iax models has their own slope due to their different ways to explode the star and their corresponding energy production. For example, the data for the C+O WD models with centered flame is more clustered near $M_{\text{Ni}} = 0.3$. This is because those data points correspond to where the star is almost completely disrupted, while the lack of the detonation bounds the possible ^{56}Ni production.

However, globally, the models show a general linear trend with dispersion. We again see at low ^{56}Ni , the pair has a linear relation to a good approximation, which can be fitted by $M_{\text{ej}} \approx 4M_{\text{Ni}}$ where we require the fitting line to pass through the origin.

Accompanying with the partial ejection of the WD materials, a small mass WD, which is bounded gravitationally, survives. The typical bounded mass ranges from 0.2 to $1.1 M_{\odot}$, depending on the explosion strength. Such white dwarf remnant is observable. WDs of mass $\sim 0.3 M_{\odot}$ are observed (See e.g. Brown et al. (2010)).

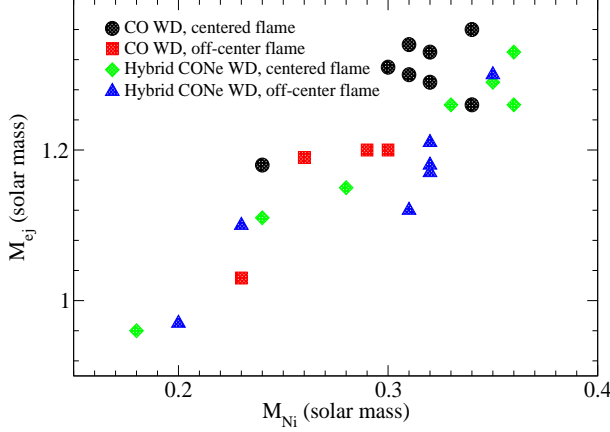


Figure 21. Ejecta mass against ejected ^{56}Ni mass for all models in this work.

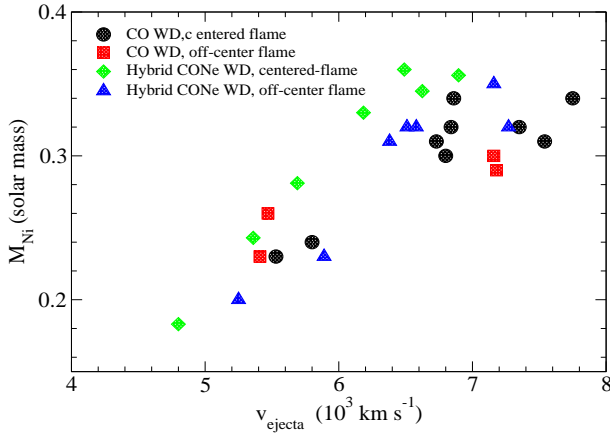


Figure 22. Ejecta ^{56}Ni mass against ejecta characteristic velocity for the SN Iax models presented in this work.

7.1.3. ^{56}Ni Mass – Ejecta Velocity Relation

At last we examine the ejecta velocity relation with ^{56}Ni production (M_{Ni}). These two quantities are associated with the observable pair Si II Velocity against absolute magnitude at peak M_V . In Figure 22 we plot the ejecta ^{56}Ni against ejecta characteristic velocity. The velocity of the ejecta v_{ejecta} is computed by first summing up the kinetic energy E_k of all the tracer particles, and then we obtain $v_{\text{ejecta}} = \sqrt{2E_k/M_{\text{ej}}}$.

We observe in this pair of observables that the ejecta velocity increases with ^{56}Ni mass linearly. The typical ejecta velocity ranges between 5000 - 8000 km s^{-1} . This corresponds to models with a strong explosion when M is large, where the energy production increases more rapidly than the growth of mass. For a given ejecta velocity, it can correspond a dispersion of ^{56}Ni mass of $\sim 0.1 M_{\odot}$ in the high velocity limit and the dispersion is smaller otherwise. This "fan"-shape pattern allows more diversity of SNe Iax when they are more luminous.

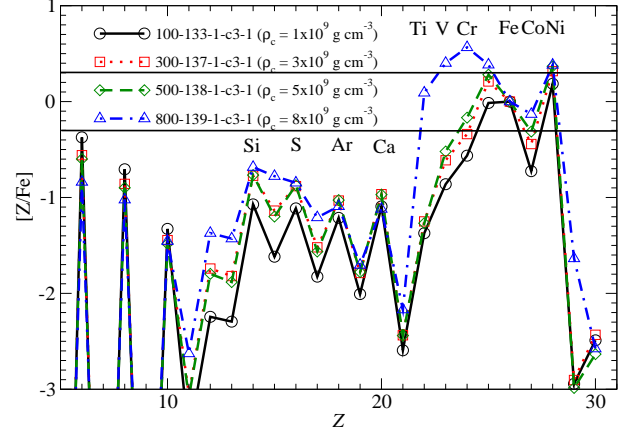


Figure 23. Ejecta chemical abundance $[Z/\text{Fe}]$ against Z for Models 100-133-1-c3-1 ($\rho_c = 1 \times 10^9 \text{ g cm}^{-3}$), 300-137-1-c3-1 ($\rho_c = 3 \times 10^9 \text{ g cm}^{-3}$), 500-138-1-c3-1 ($\rho_c = 5 \times 10^9 \text{ g cm}^{-3}$), and 800-139-1-c3-1 ($\rho_c = 8 \times 10^9 \text{ g cm}^{-3}$). All models assume C+O WD, c3-flame, $X(^{22}\text{Ne}) = 0.025$ and C/O mass fraction ratio = 1.

However, in this figure we do not attempt to directly compare our theoretical models with the observational data such as those in Foley et al. (2013). It is because to extract the reliable estimation of Si II velocity, the photosphere position and the corresponding velocity of the Si shell are essential. The exact value can be obtained by carrying out radiative transfer directly. To further relate the expected peak luminosity with the ^{56}Ni production, radiative transfer with gamma-ray energy deposition is necessary for a consistent prediction.

7.1.4. Ejecta Elemental Abundance

In typical spectral observations of SNe Iax and their remnants, the elemental abundances instead of the isotopic abundances are measured. Here we examine how the chemical abundance of SN Iax depends on the progenitor mass. By using the post-decay (i.e. after 10^6 years) stable isotopic contributions in the ejecta, we sum the mass of the isotopes of each element from C to Zn, then we compute the corresponding $[Z/\text{Fe}]$ for Models 100-133-1-c3-1 ($\rho_c = 1 \times 10^9 \text{ g cm}^{-3}$), 300-137-1-c3-1 ($\rho_c = 3 \times 10^9 \text{ g cm}^{-3}$), 500-138-1-c3-1 ($\rho_c = 5 \times 10^9 \text{ g cm}^{-3}$), and 800-139-1-c3-1 ($\rho_c = 8 \times 10^9 \text{ g cm}^{-3}$). We remind that minor long-lived radioactive isotopes still contribute but their amounts are much smaller than the major stable isotopes. These models correspond to models with different central density and hence different progenitor mass.

In Figure 23 we plot the element abundances of these models. The ejecta composition, after fallback when the hot ash pushes the external envelope and atmosphere away from the WD, appear to have a similar abundance pattern. Except Model 800-139-1-c3-1, other models

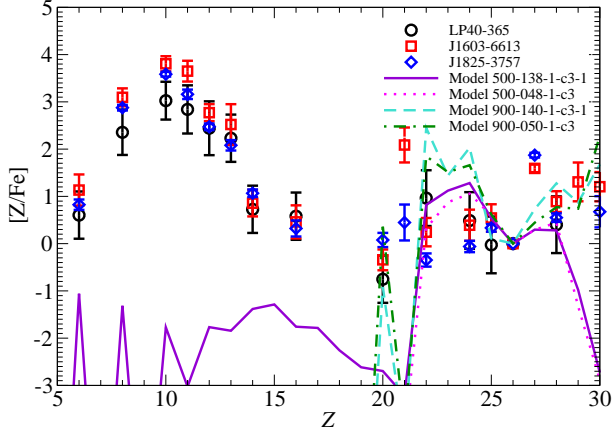


Figure 24. The abundance patterns $[Z/Fe]$ of low-mass WDs including LP40-365, J1603-6613 and J1825-3757. Representative SN Iax models including 500-138-1-c3-1, 500-047-1-c3-1, 900-140-1-c3-1 and 900-050-1-c3-1 are included for comparison.

share features including sub-solar IMEs with similar ratios of $[Ca/S]$. Light IMEs are also under-produced. It is because the turbulent flame is sub-sonic, which cannot follow the pace of expanding matter for creating an adequate amount of IMEs. The ejecta features an abundant amount of Mn, Fe and Ni with respect to the solar composition. For the contrasting model 800-139-1-c3-1, it shows a much higher Ti, V and Cr. Such difference can be the key to identify the difference in progenitor from future SNR observations.

7.2. Application to Observed Low-Mass WD

In Raddi et al. (2018, 2019) the abundance patterns are extracted from the spectra of some low-mass WDs with unusually high metal fractions. They are also traveling with a high velocity. They include LP40-365, J1603-6613 and J1825-3757.

In Figure 24 we plot the abundance patterns of these objects together with some of our representative models presented in this work. To obtain the final chemical composition, after the remnant chemical composition is obtained by post-processing, the composition in the remnant is assumed to be completely mixed. We allow the remnant to pass $\sim 10^6$ years until most typical radioactive elements have completely decayed. Exceptions include very long-lived radioactive elements such as ^{27}Al and ^{60}Fe . In this work when the radioactive decay injects energy to the remnant, the remnant is assumed to be static. No mass loss is assumed in this process.

The models include 500-138-1-c3-1, 500-050-1-c3-1, 900-140-1-c3-1 and 900-050-1-c3-1. The first two models correspond to the the C+O WD and hybrid C+O+Ne WD models with $\rho_c = 5 \times 10^9 \text{ g cm}^{-3}$. The last two

models correspond to the C+O and hybrid C+O+Ne WDs with $\rho_c = 9 \times 10^9 \text{ g cm}^{-3}$.

These observed WDs feature extremely abundant of light elements including C, O, Ne, Na, Mg and Al. These are as high as 10^4 times of the solar abundances with respect to Fe. The observed abundances of IMEs (Si, S and Ca) in these WDs are comparable with the solar abundances. It would be interesting to note that these WDs have super-solar IPEs especially Mn, Co and Ni.

Our models all show a systematic underproduction of light elements, none of which is super-solar. The IMEs are also too low compared to the objects. However, these features could originate from other reasons, e.g., the progenitors of the WDs. Possible later energy deposition due to the ^{56}Ni -decay in the remnant can also trigger further mass loss, which may further lower the Fe contribution.

The IPEs of our models appear to be similar to the observations. The values for Ti, Cr and Ni are particularly close to the observed values. We remark that the ejecta of this model shows a much higher V, but not in the remnant WD. However, none of our models can reproduce the ~ 100 times production of Co/Fe as seen in the two WDs shown here.

We note that there are SN Iax models without leaving a WD remnant. For example, Sahu et al. (2008) showed that the early and late time light curves and spectra of SN 2005hk are well-reproduced with the pure deflagration model which has no WD remnant.

Such weak explosion models can be found in PTD models with pulsation (e.g., Nomoto et al. 1976) and relatively fast flame propagation (e.g., Fink et al. 2014). The exact ejection mass depends strongly on the initial flame location. An off-center flame tends to suppress the ejected mass.

7.3. Application to Supernova Remnant

We further apply the explosion yield to some supernova remnants (SNRs). In Yamaguchi et al. (2015) the chemical abundance pattern of the SNR 3C 397 is discussed. Similar analysis has been done for various SNRs in the galaxy and in the Large Magellanic Cloud as reported in Martínez-Rodríguez et al. (2017). From the X-ray spectra, it is found that this galactic SN remnant (3C 397) contains extremely high mass ratios Mn/Fe and Ni/Fe, which hints on the possibility of super-solar metallicity of the progenitor star.

However, in Dave et al. (2017) another possibility of using the Chandrasekhar mass model in the high mass end ($\rho_c \sim 6 \times 10^9 \text{ g cm}^{-3}$) is proposed to explain the high Mn/Ni mass ratio. Here we further investigate if SN Iax models can approach this data point without invoking

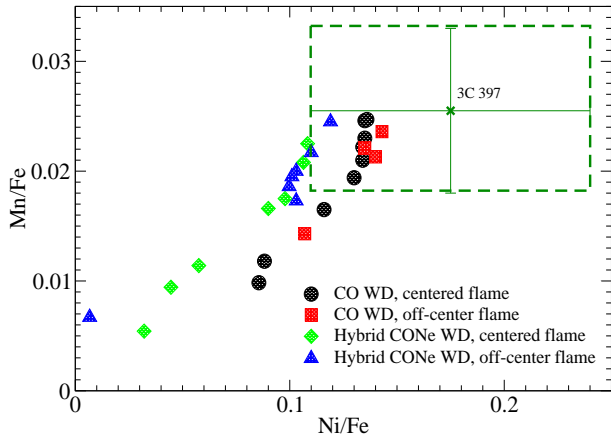


Figure 25. The mass ratios of Mn/Fe against Ni/Fe for the ejecta from C+O and hybrid C+O+Ne WD models in this work. The data point corresponds to the SN remnant 3C 397.

ing high metallicity. Also, in [Martínez-Rodríguez et al. \(2017\)](#) the Ca/S mass ratio can be the hint to understand the diversity of observed SNRs with the parameters other than metallicity. Here we examine how the central density of the WD contributes to the diversity.

In [Figure 25](#) we plot the mass ratios Mn/Fe against Ni/Fe for models in [Table 4](#). The data point corresponds to the SNR 3C 397 with the one sigma error box is shown. C+O WD models with $\rho_c > 6 \times 10^9 \text{ g cm}^{-3}$ are found in the observational error box. We remark that in PTD models, neutron-rich IPEs are synthesized by the deflagration in the central region where Y_e is determined by electron capture in NSE. Thus Mn/Fe and Ni/Fe are sensitive to the central Y_e and thus the central density, but not the initial metallicity. In DDT models, on the other hand, IPEs are produced (in addition to the central deflagration) in the detonation at the low density outer region, so that Mn/Fe and Ni/Fe are more sensitive to the initial Y_e and thus metallicity.

In [Yamaguchi et al. \(2015\)](#) the Cr/Fe mass ratio is also measured as $\text{Cr/Fe} = 0.027 \pm_{0.006}^{0.007}$. By comparing with our chemical yields listed in [Tables 4](#) and [7](#), Cr/Fe is sensitive to the central density as well. It sharply increases from ~ 0.003 in Model 100-133-1-c3-1 to ~ 0.064 in Model 900-140-1-c3-1. The best value lies around 0.029 of Model 750-139-1-c3-1 with $\rho_c = 7.5 \times 10^9 \text{ g cm}^{-3}$. Similar results appear for the hybrid C+O+Ne WD which has $\text{Cr/Fe} \sim 0.005 - 0.045$ in our sampled density range. Model 750-050-1-c3-1 with $\rho_c = 7.5 \times 10^9 \text{ g cm}^{-3}$ has the mass ratio $\text{Cr/Fe} = 0.026$ being closest to the observational data. The sharp dependence on the central density provides another precise indicator to identify the required numerical model. It suggests that by treating Cr/Fe, Mn/Fe and Ni/Fe as a three-

dimensional parameter space can largely confine the potential SN Iax model as a physical origin of SNR 3C397.

In order to judge if PTD is the origin of 3C397, further constraints apply to this object, such as the mass ratios of Ca/S and Ar/S. The observed mass ratios are $\text{Ca/S} = 0.12 - 0.16$ and $\text{Ar/S} = 0.17 - 0.18$ ([Martínez-Rodríguez et al. 2017](#)). Our models with $\rho_c \geq 5.5 \times 10^9 \text{ g cm}^{-3}$ give the mass ratios of $\text{Ca/S} = 0.08 - 0.16$ and $\text{Ar/S} = 0.14 - 0.17$ for C+O WDs and $\text{Ca/S} = 0.18 - 0.19$ and $\text{Ar/S} \sim 0.20$ for hybrid C+O+Ne WDs. The tight constraint by Ar/S is challenging to the claim that 3C 397 is an SN Iax origin. Future detection or no-detection of a low mass WD remnant will provide a definite indication to this physical picture.

Besides SNRs, the nucleosynthesis results presented in this work can be further applied to the galactic chemical evolution (e.g. [Matteucci & Greggio 1986](#); [Pagel 1997](#); [Kobayashi et al. 2020](#)) to identify the role of individual types of SNe to the trend formation of specific elements as a function of metallicity. In particular, SNe Iax can be important in dSph where the star formation history is largely different from ordinary galaxies. The unique abundance pattern of SNe Iax yields leaves observable effects. For example, in models for dSph ([Kobayashi et al. 2015, 2020](#); [Cescutti & Kobayashi 2017](#)), SNe Iax contribute to form the evolutionary trends of $[\text{Mn/Fe}]$ and $[\text{O/Fe}]$ consistently.

8. CONCLUSION

In this work we have carried out the parameter survey for the explosive nucleosynthesis in SNe Iax models using the pure turbulent deflagration model as the explosion mechanism. We explored near-Chandrasekhar mass C+O WDs and hybrid C+O+Ne WDs as the progenitors. We studied nucleosynthesis products in both the ejecta and bound remnants and their parameter dependence, including the central density of the progenitor WD, initial flame structure, initial C/O ratio, and turbulent flame speed formula for the two types of WDs. Our results are summarized as follows:

- (1) The ejecta is a mixture of burnt ash with iron-peak elements (IPEs) and unburnt C+O-rich or C+ON+Ne-rich matter.
- (2) The central density of the progenitor WD is the most important parameter for chemical compositions of the ejecta and the remnant WD. The explosion models with higher central densities enhance production of V, Cr, Fe and Ni relative to Fe by up to ~ 100 times the solar abundances in the ejecta and close to 10^3 times in the remnant WDs. The abundance in the ejecta is also sensitive to the initial flame structure. It is less sensitive to the C/O ratio and turbulent flame speed formula.

(3) The hybrid C+O+Ne WD shows similar features to the C+O WD except that the ejected mass is smaller due to the smaller nuclear energy release. The ejecta includes IPEs with similar abundance patterns to the solar, while the remnant WD contains overproduced Ti, V and Cr. IMEs such as Si, S, Ar and Ca are underproduced in both ejecta and the remnant WD.

(4) We compare the relations between the ejecta mass, explosion energy, and ^{56}Ni mass in our models. We find a linear trend for the low energy explosion up to $\sim 4 \times 10^{50}$ erg and ^{56}Ni up to $\sim 0.3 M_{\odot}$. We also examine the ^{56}Ni mass against the ejecta velocity to compare with the observational trends of SNe Iax. A clear linear trend can be observed for the ejecta mass against ejecta energy and ^{56}Ni mass in the ejecta.

(5) We further compare the model abundances with the recently observed low mass WDs: LP40-365, J1603-6613 and J1825-3757. Our models reproduce some aspects of the observed abundance pattern, especially the enhanced IPEs. The observed high abundances of Cr, Mn, and Ni are consistent with the explosion at the central density as high as $\sim 5 \times 10^9$ g cm $^{-3}$. However the high ratio [Co/Fe] cannot be reproduced.

(6) We compare our yields with the recently observed supernova remnant 3C 397, which has super-solar Mn/Fe and Ni/Fe ratios. Our SN Iax models with the central density higher than $\sim 5 \times 10^9$ g cm $^{-3}$ reproduce

the measured high Mn/Fe and Ni/Fe ratios. Thus SN Iax from a near Chandrasekhar mass WD with a high enough central density (and solar metallicity) is a possible alternative to the SN Ia with very high metallicity ($5 Z_{\odot}$) (e.g., Leung & Nomoto 2018, 2020) for the model of 3C 397. However, further accurate determination of the observed abundances may be necessary to distinguish between models for 3C 397.

9. ACKNOWLEDGMENTS

This work has been supported by the World Premier International Research Center Initiative (WPI Initiative), MEXT, Japan, and JSPS KAKENHI Grant Number JP17K05382 and JP20K04024. S.C.L. also acknowledges the support by the funding HST-AR-15021.001-A and 80NSSC18K1017.

We thank Francis Xavier Timmes for the open-source subroutines including the helmholtz equation of state, seven-isotope network and the torch nuclear reaction network. S.C.L. thanks Friedrich Roepke and Florian Lach for the insightful discussion in the topic of deflagration and flame geometry. We thank Chiaki Kobayashi for the motivation of this project from the galactic chemical evolution perspective. We thank Samuel Jones for useful discussion in nucleosynthesis. We thank Hiroya Yamaguchi about the detailed modeling of the supernova remnant 3C 397.

APPENDIX

A. OVERVIEW AND INPUT PHYSICS OF THE SIMULATION CODE

In this section we briefly review the input physics we use for modeling the SNe Iax in this article.

We use our own supernova hydrodynamics code for all the hydrodynamics simulation here. The code solves the two-dimensional Euler equations with shock-capturing scheme. The spatial discretization is obtained by the 5th-order Weighted Essentially Non-Oscillatory Scheme (Barth & Deconinck 1999) and the time discretization is obtained by the 5-step 3rd-order non-strong Stability Preserving Runge-Kutta scheme (Wang & Spiteri 2007).

We use the Helmholtz equation of state for modeling the microphysics (Timmes 1999). The equation of state describes the properties of non-interacting electron gas of arbitrarily relativistic and degenerate levels. It also contains contribution from nuclei as a classical ideal gas, photon gas in Planck distribution and electron-positron pair. The Coulomb correction is also included for the screening effects between electron gas and nuclei.

To describe the chemistry, we use the 7-isotope network identical to Timmes & Arnett (1999). This network contains ^4He , ^{12}C , ^{16}O , ^{20}Ne , ^{24}Mg , ^{28}Si and ^{56}Ni . We note that this is the most simplified network one can use to describe the nuclear reaction of CO matter and ONe matter. However, as all isotopes in this network are along the α -chain network, to accommodate the electron capture physics, we treat the mean electron mole number Y_e (also known as the electron fraction) as an independent quantity. It follows the fluid motion as a scalar quantity, but it can be modified by including the electron capture rate (see below for further discussion). With Y_e is an extra quantity, in the code, we treat the mean atomic number \bar{Z} is the implied value from the mean mass number \bar{A} and Y_e that $\bar{Z} = \bar{A}Y_e$.

Table 2. Comparison of the input physics with the works in the literature. "Hydrodynamics" is the hydrodynamics solver used for solving the Euler equations. "Dimensionality" is the number of dimension used in the simulations. "Microphysics" is the equation of state used. "E-cap scheme" is the electron capture scheme. "PP isotope no." is the number of isotopes used in the post-processing with "tracer no." is the number of passive tracers for recording the thermodynamical history. "Flame Cap" is the flame capturing scheme used for tracking the deflagration front. "Nuc. network" is the simplified network used in the hydrodynamics simulations with "3-step" for the three-step nuclear reaction scheme described in Townsley et al. (2002) and "table" for the pre-built nuclear reaction table. "Hyd isotope no." is the number of isotopes used in the hydrodynamics simulations. "SSG" is the sub-grid scale turbulence scheme used to model the development of eddy motion. "n/a" in the table means that no exact implementation details can be found.

physics	this work	Reinecke et al. (2002a)	Jones et al. (2016)	Long et al. (2014)	Fink et al. (2014)
hydrodynamics	WENO	prometheus	prometheus	FLASH	prometheus
dimensionality	2	2	3	3	3
microphysics	helmholtz	private	private	helmholtz	private
e-cap scheme	extended	n/a	extended	n/a	Seitenzahl et al. (2009)
pp isotope no.	495	n/a	384	n/a	384
tracer no.	160 ²	n/a		10 ⁷	200 ³
flame cap	level-set	level-set	level-set	3-step	level-set
nuc. network	3-step	table	table	3-step	table
Hyd isotope no.	7	5	5	3	5
SSG	one-eq. model	one-eq. model	one-eq. model	n/a	one-eq. model

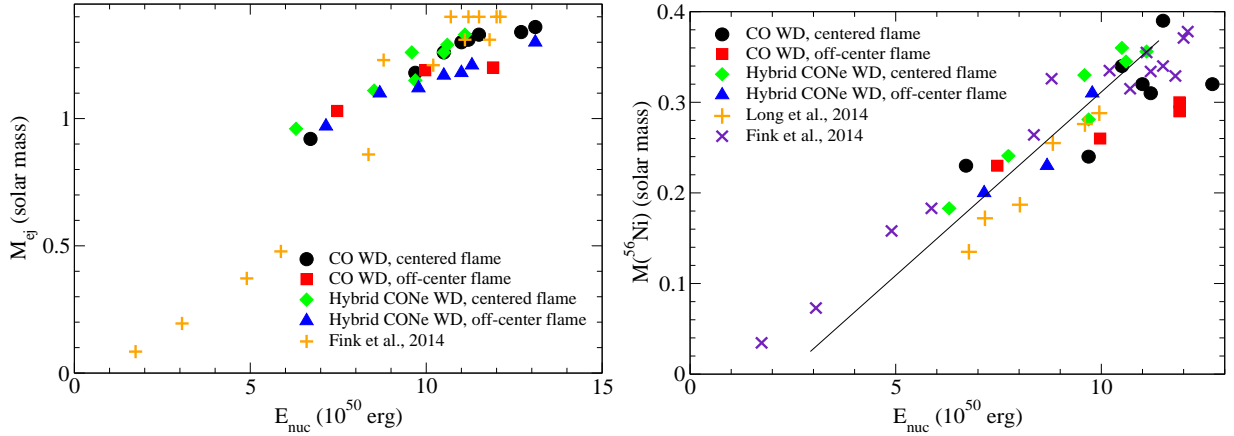


Figure 26. (left panel) The ejecta mass against the total energy released by nuclear reactions computed by our models, and in those reported in Fink et al. (2014). (right panel) Similar to the left panel but for the ^{56}Ni -mass against the total energy released by nuclear reactions and also in those reported in Fink et al. (2014); Long et al. (2014). A fitted straight line is shown to demonstrate the trend of the models.

B. COMPARISON WITH LITERATURE

B.1. Reinecke et al. (2002a) and related works

Our code has a similar structure with their works but with some distinctive differences. In Table 2 we tabulate the similarities and differences of our code compared with theirs. In general our codes are similar as we make detailed references while validating our code performance.

Our model 300-000-1-c3-1 is similar to their model c3_2d_256 in terms of resolution and initial flame structure. They have a total nuclear reaction energy of 7.19×10^{50} erg and "Ni"-production of $0.40 M_{\odot}$. $\sim 0.6 M_{\odot}$ of matter is burnt. In our model, we have a stronger explosion of 9.69×10^{50} erg released by nuclear reaction and $0.35 M_{\odot}$ of ^{56}Ni . $0.625 M_{\odot}$ of matter is burnt by the deflagration. The difference in the choice of equation of state, electron capture rate and

also the detailed implementation of sub-grid scale turbulence can contribute to the observed differences. Despite that, we obtain qualitative very similar flame structure as seen from their Figure 2.

B.2. *Jones et al. (2016)*

This work is based on the extension from [Reinecke et al. \(2002a\)](#) and the later extension in the microphysics, in particular the electron capture table for the NSE matter by including rates from e.g. [Nabi & Klapdor-Kleingrothaus \(2004\)](#). They focus on the deflagration phase of the ONe core in the context of electron capture supernova evolved super-AGB stars ([Jones et al. 2013](#)).

Their three-dimensional code allows them to explore complex off-center flame structure. Their model G15 is similar to our Model 900-140-1-c3-1 (in Appendix) but differ by flame structure owing to their three-dimensional freedom in flame placement. They observe ejecta and remnant masses of 0.177 and 1.212 M_{\odot} . On the other hand we observe a larger ejecta mass by 0.567 M_{\odot} . The difference might be originated from the initial flame we use (c3 flame), which is extended in size ~ 100 km. This also enhances the energy release by deflagration. Also, its aspherical shape facilitates the turbulence production and hence the amount of matter burnt at early time. This suppresses the initial electron capture effect.

B.3. *Long et al. (2014)*

This code uses another code FLASH for modeling the deflagration phase of SNe Ia. Again, we tabulate their input physics in Table 2. Major differences of this code is that the flame propagation does not depend on sub-grid scale turbulence, but only Rayleigh-Taylor instabilities. Notice that such instabilities depend on local gravity g . Near the core, the local gravity scales as $g(r) \sim m(r)/r^2 \sim \rho r \rightarrow 0$. This means the flame is almost like laminar near the center. On the other hand, there is no such restriction in sub-grid scale turbulence model. As long as the shear-stress is strong, eddy motion can be generated anywhere inside the star which accelerates the flame propagation.

[Long et al. \(2014\)](#) construct a WD of mass 1.365 M_{\odot} with equal mass fractions of ^{12}C and ^{16}O . Again, the use of three-dimensional hydrodynamics offers the possibility to explore off-center bubble flame structure.

Due to the weaker flame propagation, they observe a higher bound mass for the same amount of bubbles used, when compared with [Fink et al. \(2014\)](#). We notice the drastic difference in the flame structure. While flame structure affects strongly the explosion energetics in three-dimensional simulation, we only compare with the global trends of their models. We do not compare the ejecta mass because we cannot find the corresponding numbers.

In the right panel of Figure 26 we plot the ^{56}Ni -mass in the ejecta against nuclear energy release of all models. We can see a very consistent trend between our work and their work. This suggests that our code can capture a consistent result in following how the energy input from deflagration contributes to the final ejecta mass. Our models show also a narrow band as theirs which can reach as high as M_{Ni} . This means that in the high-mass regime, the faster and stronger nuclear flame is balanced by other effects, such as the electron capture effects. The production of ^{56}Ni therefore becomes saturated. However, our models does not show that E_{nuc} reaches as low as theirs. Such models will need further exploration of three-dimensional flame structure where much smaller initial flame in the form of a few bubbles is used.

B.4. *Fink et al. (2014)*

Similar to [Seitenzahl et al. \(2013\)](#), [Fink et al. \(2014\)](#) carried out a parameter survey for the pure turbulent deflagration for the near-Chandrasekhar mass Model in three-dimensions. The code structure inherits from previous version such as [Reinecke et al. \(2002a\)](#) but with updated turbulence calculation described in ([Schmidt et al. 2006](#)). A wide range of flame structure from 1 bubble to 1600 bubbles are used to study their effects on the chemical abundance pattern and its observable. The progenitor has a central density $2.9 \times 10^9 \text{ g cm}^{-3}$ and a composition of $X(^{12}\text{C})=0.475$, $X(^{16}\text{O})=0.5$ and $X(^{22}\text{Ne})=0.025$. The ejecta mass increases from $\sim 0.08 M_{\odot}$ to complete disruption ($= 1.4 M_{\odot}$) when bubble count exceeds 150.

Since it is difficult to compare models with a different flame structure, we compare the global trends of their models with ours. In their models they show that the ejecta mass increases almost linearly with the explosion energy. We also plot the explosion energetics of their models in both panels of Figure 26.

In the left panel, we plot the relation between the ejecta mass and the total nuclear energy released. We see a very clear linear trend in our models. Their models also show a similar trend but with a lower end and higher end of the ejecta mass. Despite the difference in the range, the slope, which characterizes how the deflagration contributes to

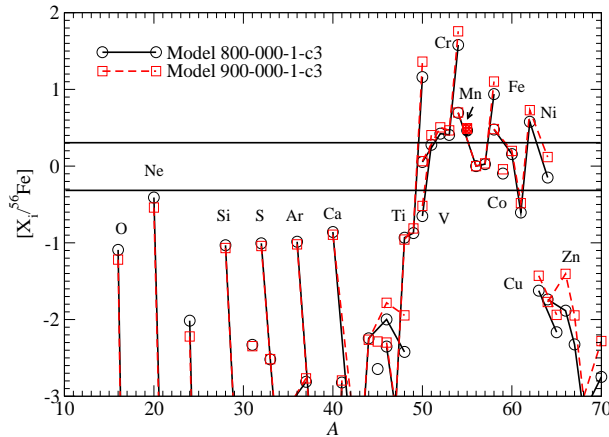


Figure 27. $[X_i / ^{56}\text{Fe}]$ against mass number for the ejecta of O+Ne+Mg WD models for 800-000-1-c3-1 ($\rho_c \approx 10^{9.9} \text{ g cm}^{-3}$) and 900-000-1-c3-1 ($\rho_c \approx 10^{9.95} \text{ g cm}^{-3}$). All models assume O+Ne+Mg composition with, $X(^{22}\text{Ne}) = 0.025$ and c3 initial flame.

the mass ejection, agrees with each other in the high E_{nuc} limit. Furthermore, our models are confined in a narrow bin from the fitted straight line. But we also notice for model with $E_{\text{nuc}} < 10^{51}$ erg, their model has a steeper slope than ours. We notice that the diversity of their model depends on the initial flame instead of the progenitor mass. A centered flame like ours provides a sufficiently large surface area to maintain burning before the expansion quenches the deflagration wave. Therefore our models tend to cluster in the strong explosion side while in their work the models span from weak explosions to strong explosions.

In the right panel, we make a similar plot to the left panel but for the ^{56}Ni -mass production. Again the trends among all works show a promising similarity. The models in their work show again the lower ^{56}Ni -mass in the lower end. Their models show a similar ^{56}Ni -mass in the upper end. The consistency in the slope, as well as the thin band formed by all the models, show that our code agree well with their hydrodynamics and post-process results.

C. O+NE+MG WD

In the main text we have presented a detailed description about how the nucleosynthesis varies with the model parameters of a C+O WD and a hybrid C+O+Ne WD. In fact, super-AGB star with a mass $8 - 10M_{\odot}$ can also form a massive O+Ne+Mg WD, where the core or shell O-burning is ignited by by electron capture and can trigger oxygen deflagration.

The outcome of the oxygen deflagration is most sensitive to the central density of the WD when the deflagration is initiated, which is called as the deflagration density $\rho_{c,\text{def}}$. This is because electron capture on NSE materials leads to the collapse of the WD, while nuclear energy release by the oxygen deflagration leads to the expansion.

Zha et al. (2019) investigated how $\rho_{c,\text{def}}$ depends on the electron capture rate, nuclear reaction rate, URCA process, and convective criterion and concluded $\log_{10}(\rho_{c,\text{def}}/\text{g cm}^{-3}) > 10.10$ is most likely. Such high $\rho_{c,\text{def}}$ has been found to lead to collapse to form a neutron star rather than thermonuclear explosion (Leung et al. 2020; Zha et al. 2019).

Earlier Jones et al. (2016, 2019) have found the the outcome for $\log_{10}(\rho_{c,\text{def}}/\text{g cm}^{-3}) = 9.95$ is thermonuclear explosion that leaves a small mass WD behind, being similar to PTD models presented in the main text.

Although we think the collapse is the likely outcome of oxygen deflagration in the actually O+Ne+Mg WDs with $\log_{10}(\rho_{c,\text{def}}/\text{g cm}^{-3}) > 10.10$, we perform numerical experiments of the pure oxygen deflagration at lower $\rho_{c,\text{def}}$, i.e., $\log_{10}(\rho_{c,\text{def}}/\text{g cm}^{-3}) = 9.95$ and 9.90 for the purpose of comparisons with Jones et al. (2016) and with the similar $\rho_{c,\text{def}}$ as C+O and C+O+Ne WD models.

In this section, we examine the explosive nucleosynthesis of the O+Ne+Mg WD. In Table 9, 10 and 11 we tabulate the nucleosynthesis yield and the radioactive isotopes in the ejecta.

C.1. Ejecta of O+Ne+Mg WD

C.1.1. Dependence on Central Density

Here we compare the nucleosynthesis pattern of O+Ne+Mg WD models of different central densities. For our numerical experiments, we adopt the ρ_c range from $10^{9.90-9.95} \text{ g cm}^{-3}$ (i.e. $8 - 9 \times 10^9 \text{ g cm}^{-3}$). Higher ρ_c in general result in a collapse to form a neutron star.

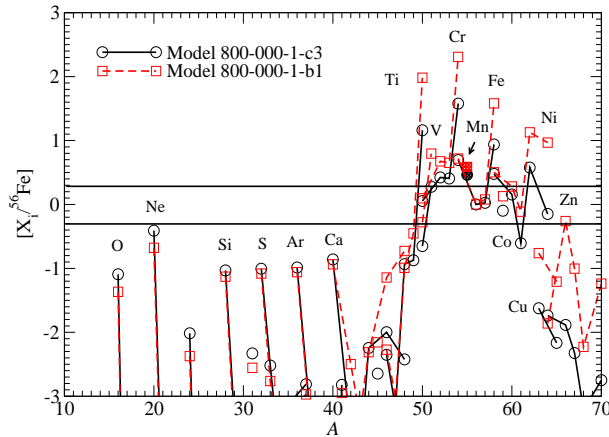


Figure 28. $[X_i/^{56}\text{Fe}]$ against mass number for the ejecta of pure O+Ne WD models for 800-000-1-c3-1 (*c3* flame) and 800-000-1-b1-1 (*b1* flame). All models assume $\rho_c = 10^{9.90} \times 10^9 \text{ g cm}^{-3}$, O+Ne+Mg composition and $X(^{22}\text{Ne}) = 0.025$.

We compare in Figure 27 the ejecta chemical composition of Models 800-000-1-c3-1 and 900-000-1-c3-1. Notice that the typical explosion of the O+Ne+Mg WD is weaker than the C+O counterpart because the nuclear energy release from O+Ne+Mg matter to NSE is smaller than the energy release from C+O matter to NSE.

The central density plays an important role in the ejecta composition for the O+Ne+Mg WD case. IMEs are underproduced and most IPEs are significantly produced. The models show to have a similar composition except that the lower mass one shows a higher yield of ^{50}Ti , $^{50-51}\text{V}$, ^{54}Cr , ^{58}Fe and $^{60,62}\text{Ni}$. During the fallback of matter in the inner layer, most IPEs including neutron-rich isotopes are trapped in the remnant. Also, the higher density WD is more compact, thus the inner layer requires a higher escape velocity for mass ejection. As a result, a larger amount of the inner part of matter is trapped, which suppresses the increase in neutron-rich isotopes.

C.1.2. Dependence on Initial Flame Structure

Here we compare the nucleosynthesis yield of the O+Ne+Mg WD models with different initial flame. In Figure 28 we plot $[X_i/^{56}\text{Fe}]$ for Models 800-000-1-c3-1 and 800-000-1-b1-1.

The ejecta properties are significantly different when the flame starts from off-center. Major isotopes of IPEs are similar. But the amount of neutron-rich isotopes can be 1 – 2 orders of magnitudes higher for the off-center flame than the centered flame. This is because the outer flame can channel the ash outwards at an earlier time, which allows more matter containing neutron-rich isotopes to escape from the gravitational pull of the star. On the other hand, IMEs are only mildly changed.

C.2. Remnant White Dwarf

C.2.1. Dependence on Central Density

We compare the remnant composition for O+Ne+Mg WDs with different ρ_c by comparing Models 800-000-1-c3-1 and 900-000-1-c3-1. In Figure 29, we plot $[X_i/^{56}\text{Fe}]$ for these two models. The remnant WD exhibits very peculiar abundance as also seen in the high density models of C+O and C+O+Ne WDs, where IPEs can be 10^3 times higher than the solar value. The different central densities provides a very different abundance pattern in the remnant WD. The lower density model (800-000-1-c3) has a much higher neutron-rich isotopes of IPEs than the higher density model (900-000-1-c3) in the remnant WD. They can be $\sim 10^{3-4}$ times higher than the solar ratios. Also, there is no observable amount of IMEs. Meanwhile, Model 900-000-1-c3 shows the abundance pattern closer to the solar composition. The IMEs are underproduced at a level of $\sim 10\%$ of the solar values. The most overproduced isotope is ^{54}Cr and it is only ~ 100 times higher, which is almost two orders of magnitude lower than that in Model 800-000-1-c3.

C.2.2. Dependence on Initial Flame Structure

In Figure 30 we compare the abundance pattern for the remnant part of Models 800-000-1-c3-1 and 800-000-1-b1-1. The remnant in the centered flame model has no observable O+Ne+Mg-rich matter or IMEs. The overproduction of IPEs, especially neutron-rich isotopes, are similar to the high density C+O and hybrid C+O+Ne models. However, the off-center model has more neutron-rich isotopes than the centered flame model. Again, in such a high density,

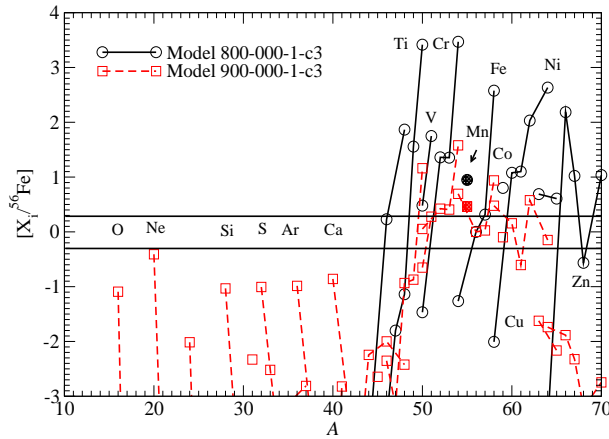


Figure 29. $[X_i/^{56}\text{Fe}]$ against mass number for the bounded remnant of O+Ne+Mg WD models for Models 800-000-1-c3-1 ($\rho_c \approx 10^{9.9} \text{ g cm}^{-3}$) and 900-000-1-c3-1 ($\rho_c \approx 10^{9.95} \text{ g cm}^{-3}$). All models assume O+Ne+Mg composition with $X(^{22}\text{Ne}) = 0.025$ and c3 initial flame.

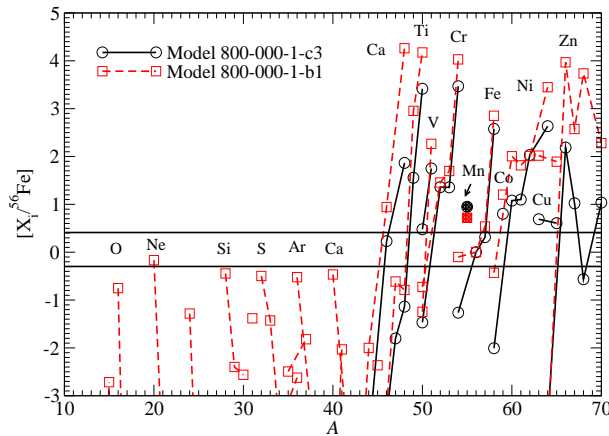


Figure 30. $[X_i/^{56}\text{Fe}]$ against atomic mass for the remnant of O+Ne+Mg WD models for 800-000-1-c3-1 (c3 flame) and 800-000-1-b1-1 (b1 flame). All models assume $\rho_c = 10^{9.90} \text{ g cm}^{-3}$, O+Ne+Mg composition with $X(^{22}\text{Ne}) = 0.025$.

electron capture begins to be important to the global dynamics as it suppresses the pressure jump after the matter is burnt. The ejecta in the centered flame is more suppressed than the ejecta in the off-center flame.

REFERENCES

- Asplund, M., Grevesse, N., Sauval, A. J., & Scott, P. 2009, *ARA&A*, 47, 481
- Barth, T. J., & Deconinck, H. 1999, *Lecture Notes in Computational Science and Engineering 9: High-Order Methods for Computational Physics* (Springer)
- Bell, J. B., Day, M. S., Rendleman, C. A., Woosley, S. E., & Zingale, M. 2004a, *Astrophys. J.*, 606, 1029
- . 2004b, *Astrophys. J.*, 608, 883
- Benvenuto, O. G., Panei, J. A., Nomoto, K., Kitamura, H., & Hachisu, I. 2015, *ApJL*, 809, L6
- Branch, D., Thomas, R. C., Baron, E., et al. 2004, *ApJ*, 606, 413
- Brooks, J., Schwab, J., Bildsten, L., Quataert, E., & Paxton, B. 2017, *ApJL*, 834, L9
- Brown, W. R., Kilic, M., Allende Prieto, C., & Kenyon, S. J. 2010, *ApJ*, 723, 1072
- Calder, A. C., Townsley, D. M., Seitenzahl, I. R., et al. 2007, *Astrophys. J.*, 656, 313
- Cescutti, G., & Kobayashi, C. 2017, *A&A*, 607, A23
- Clement, M. J. 1993, *ApJ*, 406, 651
- Dave, P., Kashyap, R., Fisher, R., et al. 2017, *ApJ*, 841, 58
- Denissenkov, P. A., Herwig, F., Truran, J. W., & Paxton, B. 2013, *ApJ*, 772, 37
- Fink, M., Kromer, M., Seitenzahl, I. R., et al. 2014, *MNRAS*, 438, 1762

- Foley, R. J., Chornock, R., Filippenko, A. V., et al. 2009, *AJ*, 138, 376
- Foley, R. J., Challis, P. J., Chornock, R., et al. 2013, *ApJ*, 767, 57
- Foley, R. J., Pan, Y.-C., Brown, P., et al. 2016, *MNRAS*, 461, 1308
- Gamezo, V. N., Khokhlov, A. M., & Oran, E. S. 2004, *PhRvL*, 92, 211102
- García-Berro, E., & Lorén-Aguilar, P. 2017, in *Handbook of Supernovae*, ed. A. W. Alsabti & P. Murdin (Cham: Springer International Publishing AG), 1237
- Hicks, E. P. 2015, *Astrophys. J.*, 803, 72
- Hoeflich, P. 2017, in *Handbook of Supernovae*, ed. A. W. Alsabti & P. Murdin, 1151
- Iwamoto, K., Brachwitz, F., Nomoto, K., et al. 1999, *Astrophys. J. Suppl.*, 125, 439
- Jackson, A. P., Townsley, D. M., & Calder, A. C. 2014, *ApJ*, 784, 174
- Jha, S. W. 2017, in *Handbook of Supernovae*, ed. A. W. Alsabti & P. Murdin (Cham: Springer International Publishing AG), 375
- Jiang, J.-a., Doi, M., Maeda, K., & Shigeyama, T. 2018, *ApJ*, 865, 149
- Jones, S., Röpke, F. K., Pakmor, R., et al. 2016, *A&A*, 593, A72
- Jones, S., Hirschi, R., Nomoto, K., et al. 2013, *ApJ*, 772, 150
- Jones, S., Röpke, F. K., Fryer, C., et al. 2019, *A&A*, 622, A74
- Jordan, G. C. I., Perets, H. B., Fisher., R. T., et al. 2012, *Astrophys. J.*, 759, 53
- Kawabata, M., Kawabata, K. S., Maeda, K., et al. 2018, *PASJ*, 70, 111
- Kobayashi, C., Leung, S.-C., & Nomoto, K. 2020, *ApJ*, 895, 138
- Kobayashi, C., Nomoto, K., & Hachisu, I. 2015, *ApJL*, 804, L24
- Kromer, M., Fink, M., Stanishev, V., et al. 2013, *MNRAS*, 429, 2287
- Kromer, M., Ohlmann, S. T., Pakmor, R., et al. 2015, *MNRAS*, 450, 3045
- Lecoanet, D., Schwab, J., Quataert, E., et al. 2016, *ApJ*, 832, 71
- Leung, S.-C., Chu, M.-C., & Lin, L.-M. 2015, *Mon. Not. R. astr. Soc.*, 454, 1238
- Leung, S.-C., & Nomoto, K. 2017a, *Mem. Soc. Astron. Italiana*, 88, 266
- Leung, S.-C., & Nomoto, K. 2017b, in *14th International Symposium on Nuclei in the Cosmos (NIC2016)*, ed. S. Kubono, T. Kajino, S. Nishimura, T. Isobe, S. Nagataki, T. Shima, & Y. Takeda, 020506
- . 2018, *ApJ*, 861, 143
- . 2019, *PASA*, 36, e006
- . 2020, *ApJ*, 888, 80
- Leung, S.-C., Nomoto, K., & Suzuki, T. 2020, *ApJ*, 889, 34
- Leung, S.-C., Zha, S., Chu, M.-C., Lin, L.-M., & Nomoto, K. 2019, *ApJ*, 884, 9
- Li, W., Filippenko, A. V., Treffers, R. R., et al. 2001, *ApJ*, 546, 734
- Li, W., Filippenko, A. V., Chornock, R., et al. 2003, *PASP*, 115, 453
- Livne, E. 1993, *ApJL*, 406, L17
- Livne, E., & Arnett, D. 1993, *ApJL*, 415, L107
- Long, M., Jordan, George C. I., van Rossum, D. R., et al. 2014, *ApJ*, 789, 103
- Martínez-Rodríguez, H., Badenes, C., Yamaguchi, H., et al. 2017, *ApJ*, 843, 35
- Matteucci, F., & Greggio, L. 1986, *A&A*, 154, 279
- Nabi, J.-U., & Klapdor-Kleingrothaus, H. V. 2004, *Atomic Data and Nuclear Data Tables*, 88, 237
- Niemeyer, J. C., & Hillebrandt, W. 1995, *ApJ*, 452, 779
- Niemeyer, J. C., Hillebrandt, W., & Woosley, S. E. 1995, *Astrophys. J.*, 452, 769
- Niemeyer, J. C., & Woosley, S. E. 1997, *ApJ*, 475, 740
- Nomoto, K. 1982a, *Astrophys. J.*, 253, 798
- . 1982b, *Astrophys. J.*, 257, 780
- Nomoto, K. 1984, *ApJ*, 277, 791
- . 1987, *ApJ*, 322, 206
- Nomoto, K., Kobayashi, C., & Tominaga, N. 2013, *Annu. Rev. Astron. and Astrophys.*, 51, 457
- Nomoto, K., & Leung, S.-C. 2017a, in *Handbook of Supernovae*, ed. A. W. Alsabti & P. Murdin (Cham: Springer International Publishing AG), 1275
- . 2017b, in *Handbook of Supernovae*, ed. A. W. Alsabti & P. Murdin (Cham: Springer International Publishing AG), 483
- . 2018, *SSRv*, 214, 67
- Nomoto, K., Sugimoto, D., & Neo, S. 1976, *Ap & SS*, 39, 37
- Nomoto, K., Thielemann, F.-K., & Yokoi, K. 1984, *Astrophys. J.*, 286, 644
- Osher, S., & Sethian, J. A. 1988, *Journal of Computational Physics*, 79, 12
- Pagel, B. E. J. 1997, *Nucleosynthesis and Chemical Evolution of Galaxies*
- Pakmor, R. 2017, *Violent Mergers*, ed. A. W. Alsabti & P. Murdin, 1257

- Perlmutter, S., Gabi, S., Goldhaber, G., et al. 1997, *ApJ*, 483, 565
- Phillips, M. M. 1993, *ApJL*, 413, L105
- Phillips, M. M., Li, W., Frieman, J. A., et al. 2007, *PASP*, 119, 360
- Pocheau, A. 1994, *Phys. Rev. E*, 49, 1109
- Raddi, R., Hollands, M. A., Koester, D., et al. 2018, *ApJ*, 858, 3
- . 2019, *MNRAS*, 1623
- Reinecke, M., Hillebrandt, W., & Niemeyer, J. C. 1999a, *Astron. Astrophys.*, 347, 739
- . 2002a, *Astron. Astrophys.*, 386, 936
- . 2002b, *Astron. Astrophys.*, 391, 1167
- Reinecke, M., Hillebrandt, W., Niemeyer, J. C., Klein, R., & Gloebl, A. 1999b, *Astron. Astrophys.*, 347, 724
- Riess, A. G., Press, W. H., & Kirshner, R. P. 1996, *ApJ*, 473, 88
- Röpke, F. K. 2005, *Astron. Astrophys.*, 432, 969
- Röpke, F. K. 2017, in *Handbook of Supernovae*, ed. A. W. Alsabti & P. Murdin, 1185
- Röpke, F. K., Gieseler, M., Reinecke, M., Travaglio, C., & Hillebrandt, W. 2006a, *A&A*, 453, 203
- Röpke, F. K., & Hillebrandt, W. 2005, *Astron. Astrophys.*, 431, 635
- Röpke, F. K., Hillebrandt, W., & Niemeyer, J. C. 2004a, *Astron. Astrophys.*, 421, 411
- . 2004b, *Astron. Astrophys.*, 421, 783
- Röpke, F. K., Hillebrandt, W., Niemeyer, J. C., & Woosley, S. E. 2006b, *A&A*, 448, 1
- Röpke, F. K., Hillebrandt, W., Schmidt, W., et al. 2007, *ApJ*, 668, 1132
- Sahu, D. K., Tanaka, M., Anupama, G. C., et al. 2008, *ApJ*, 680, 580
- Schmidt, W., Niemeyer, J. C., Hillebrandt, W., & Röpke, F. K. 2006, *Astron. Astrophys.*, 450, 283
- Seitenzahl, I. R., Taubenberger, S., & Sim, S. A. 2009, *MNRAS*, 400, 531
- Seitenzahl, I. R., Ciaraldi-Schoolmann, F., Röpke, F. K., et al. 2013, *MNRAS*, 429, 1156
- Taubenberger, S. 2017, in *Handbook of Supernovae*, ed. A. W. Alsabti & P. Murdin (Cham: Springer International Publishing AG), 317
- Timmes, F. X. 1992, *Astrophys. J.*, 423, L131
- . 1999, *Astrophys. J.*, 124, 241
- Timmes, F. X., & Arnett, D. 1999, *Astrophys. J.*, 125, 277
- Timmes, F. X., Hoofman, R. D., & Woosley, S. E. 2000, *Astrophys. J. Suppl.*, 129, 377
- Timmes, F. X., & Woosley, S. E. 1992, *Astrophys. J.*, 396, 649
- Townsley, D. M., Calder, A. M., Asida, S. M., et al. 2002, *Astrophys. J. Suppl.*, 143, 201
- Townsley, D. M., Miles, B. J., Timmes, F. X., Calder, A. C., & Brown, E. F. 2016, *Astrophys. J. Suppl.*, 225, 3
- Travaglio, C., Hillebrandt, W., Reinecke, M., Thielemann, F.-K., et al. 2004, *Astrophys. J.*, 425, 1029
- Tsuruta, S., Leung, S.-C., & Nomoto, K. 2018, *International Journal of Modern Physics D*, 27, 1830004
- Wang, R., & Spiteri, R. J. 2007, *SIAM J. Numer. Anal.*, 45, 1871
- Woosley, S. E. 1997, *ApJ*, 476, 801
- Yamaguchi, H., Badenes, C., Foster, A. R., et al. 2015, *ApJL*, 801, L31
- Zha, S., Leung, S.-C., Suzuki, T., & Nomoto, K. 2019, *ApJ*, 886, 22

Table 3. Mass of major isotopes in the ejecta after all short-lived radioactive isotopes have decayed. The isotope masses are in units of solar mass.

Isotopes	100-133-1-c3-1	200-135-1-c3-1	300-137-1-c3-1	500-138-1-c3-1	550-138-1-c3-1	750-139-1-c3-1	900-140-1-c3-1
¹² C	2.96×10^{-1}	3.81×10^{-1}	3.21×10^{-1}	3.14×10^{-1}	3.14×10^{-1}	2.43×10^{-1}	1.82×10^{-1}
¹³ C	6.56×10^{-12}	4.44×10^{-11}	6.50×10^{-11}	6.55×10^{-11}	5.31×10^{-11}	1.42×10^{-10}	2.9×10^{-10}
¹⁴ N	9.12×10^{-10}	3.85×10^{-9}	5.85×10^{-9}	5.37×10^{-9}	4.72×10^{-9}	1.23×10^{-8}	1.87×10^{-8}
¹⁵ N	2.77×10^{-10}	1.44×10^{-9}	1.44×10^{-9}	1.29×10^{-9}	1.43×10^{-9}	3.17×10^{-9}	4.53×10^{-9}
¹⁶ O	3.1×10^{-1}	4.8×10^{-1}	3.54×10^{-1}	3.44×10^{-1}	3.40×10^{-1}	3.17×10^{-1}	2.82×10^{-1}
¹⁷ O	2.96×10^{-10}	1.33×10^{-9}	2.9×10^{-9}	1.93×10^{-9}	1.70×10^{-9}	4.41×10^{-9}	6.78×10^{-9}
¹⁸ O	9.15×10^{-12}	3.86×10^{-11}	6.27×10^{-11}	5.59×10^{-11}	5.2×10^{-11}	1.29×10^{-10}	1.99×10^{-10}
¹⁹ F	3.57×10^{-12}	1.52×10^{-11}	1.81×10^{-11}	1.75×10^{-11}	1.65×10^{-11}	4.23×10^{-11}	6.14×10^{-11}
²⁰ Ne	7.40×10^{-4}	3.10×10^{-3}	3.23×10^{-3}	3.17×10^{-3}	3.17×10^{-3}	8.1×10^{-3}	1.11×10^{-2}
²¹ Ne	2.46×10^{-8}	1.3×10^{-7}	1.8×10^{-7}	1.12×10^{-7}	1.3×10^{-7}	2.80×10^{-7}	3.88×10^{-7}
²² Ne	1.20×10^{-2}	1.55×10^{-2}	1.31×10^{-2}	1.28×10^{-2}	1.28×10^{-2}	9.90×10^{-3}	7.43×10^{-3}
²³ Na	2.20×10^{-6}	9.76×10^{-6}	1.5×10^{-5}	1.5×10^{-5}	1.2×10^{-5}	2.49×10^{-5}	3.62×10^{-5}
²⁴ Mg	7.48×10^{-4}	3.58×10^{-3}	3.99×10^{-3}	3.75×10^{-3}	3.44×10^{-3}	9.1×10^{-3}	1.18×10^{-2}
²⁵ Mg	5.9×10^{-6}	1.98×10^{-5}	2.20×10^{-5}	2.13×10^{-5}	2.6×10^{-5}	5.39×10^{-5}	7.45×10^{-5}
²⁶ Mg	7.24×10^{-6}	3.14×10^{-5}	3.35×10^{-5}	3.28×10^{-5}	3.20×10^{-5}	8.3×10^{-5}	1.14×10^{-4}
²⁶ Al	2.39×10^{-29}	3.6×10^{-29}	3.27×10^{-29}	9.62×10^{-10}	9.33×10^{-10}	2.54×10^{-9}	3.53×10^{-29}
²⁷ Al	6.4×10^{-5}	2.67×10^{-4}	3.1×10^{-4}	2.78×10^{-4}	2.59×10^{-4}	7.23×10^{-4}	9.40×10^{-4}
²⁸ Si	1.21×10^{-2}	3.64×10^{-2}	4.0×10^{-2}	4.36×10^{-2}	3.61×10^{-2}	5.5×10^{-2}	6.3×10^{-2}
²⁹ Si	6.71×10^{-5}	3.9×10^{-4}	3.51×10^{-4}	3.36×10^{-4}	2.97×10^{-4}	8.21×10^{-4}	1.10×10^{-3}
³⁰ Si	9.78×10^{-5}	4.89×10^{-4}	5.78×10^{-4}	5.34×10^{-4}	4.62×10^{-4}	1.36×10^{-3}	1.78×10^{-3}
³¹ P	2.52×10^{-5}	1.6×10^{-4}	1.27×10^{-4}	1.17×10^{-4}	1.0×10^{-4}	2.98×10^{-4}	3.92×10^{-4}
³² S	6.28×10^{-3}	1.61×10^{-2}	1.75×10^{-2}	1.92×10^{-2}	1.58×10^{-2}	1.97×10^{-2}	2.25×10^{-2}
³³ S	1.99×10^{-5}	7.75×10^{-5}	9.38×10^{-5}	8.88×10^{-5}	7.29×10^{-5}	2.23×10^{-4}	2.91×10^{-4}
³⁴ S	1.6×10^{-4}	5.7×10^{-4}	6.13×10^{-4}	6.2×10^{-4}	4.76×10^{-4}	1.8×10^{-3}	1.47×10^{-3}
³⁶ S	1.2×10^{-8}	4.88×10^{-8}	5.80×10^{-8}	5.46×10^{-8}	4.62×10^{-8}	1.52×10^{-7}	1.97×10^{-7}
³⁵ Cl	1.11×10^{-5}	3.30×10^{-5}	3.82×10^{-5}	3.62×10^{-5}	3.24×10^{-5}	7.73×10^{-5}	1.6×10^{-4}
³⁷ Cl	1.84×10^{-6}	5.6×10^{-6}	5.83×10^{-6}	6.19×10^{-6}	4.75×10^{-6}	8.54×10^{-6}	1.10×10^{-5}
³⁶ Ar	1.15×10^{-3}	2.60×10^{-3}	2.83×10^{-3}	3.6×10^{-3}	2.53×10^{-3}	2.69×10^{-3}	2.89×10^{-3}
³⁸ Ar	6.68×10^{-5}	2.33×10^{-4}	2.71×10^{-4}	2.83×10^{-4}	2.21×10^{-4}	2.87×10^{-4}	3.46×10^{-4}
⁴⁰ Ar	1.71×10^{-10}	6.25×10^{-10}	7.50×10^{-10}	6.68×10^{-10}	5.94×10^{-10}	2.42×10^{-9}	3.11×10^{-9}
³⁹ K	6.49×10^{-6}	1.64×10^{-5}	1.82×10^{-5}	1.98×10^{-5}	1.49×10^{-5}	1.96×10^{-5}	2.61×10^{-5}
⁴⁰ K	3.89×10^{-9}	9.94×10^{-9}	1.19×10^{-8}	1.3×10^{-8}	9.65×10^{-9}	3.31×10^{-8}	4.39×10^{-8}
⁴¹ K	4.85×10^{-7}	1.9×10^{-6}	1.14×10^{-6}	1.27×10^{-6}	9.28×10^{-7}	1.17×10^{-6}	1.47×10^{-6}
⁴⁰ Ca	1.4×10^{-3}	2.12×10^{-3}	2.34×10^{-3}	2.47×10^{-3}	2.5×10^{-3}	1.98×10^{-3}	1.97×10^{-3}
⁴² Ca	2.28×10^{-6}	6.57×10^{-6}	7.47×10^{-6}	7.98×10^{-6}	6.8×10^{-6}	8.44×10^{-6}	1.3×10^{-5}
⁴³ Ca	7.46×10^{-9}	1.55×10^{-8}	2.24×10^{-8}	1.92×10^{-8}	1.62×10^{-8}	5.71×10^{-8}	7.92×10^{-8}
⁴⁴ Ca	8.41×10^{-7}	1.40×10^{-6}	1.87×10^{-6}	1.84×10^{-6}	1.56×10^{-6}	1.84×10^{-6}	2.3×10^{-6}
⁴⁶ Ca	2.80×10^{-12}	9.47×10^{-12}	1.29×10^{-11}	1.31×10^{-11}	2.82×10^{-10}	6.17×10^{-9}	4.36×10^{-8}
⁴⁸ Ca	1.68×10^{-17}	5.34×10^{-17}	6.59×10^{-17}	2.66×10^{-14}	2.3×10^{-11}	3.11×10^{-9}	1.78×10^{-6}
⁴⁵ Sc	1.84×10^{-8}	3.64×10^{-8}	4.41×10^{-8}	4.68×10^{-8}	3.63×10^{-8}	7.75×10^{-8}	9.94×10^{-8}
⁴⁶ Ti	1.6×10^{-6}	2.86×10^{-6}	3.20×10^{-6}	3.64×10^{-6}	2.65×10^{-6}	3.27×10^{-6}	3.98×10^{-6}
⁴⁷ Ti	4.20×10^{-8}	7.71×10^{-8}	1.6×10^{-7}	1.10×10^{-7}	9.56×10^{-8}	1.96×10^{-7}	2.77×10^{-7}
⁴⁸ Ti	2.22×10^{-5}	3.68×10^{-5}	4.80×10^{-5}	4.75×10^{-5}	4.42×10^{-5}	4.97×10^{-5}	5.6×10^{-5}
⁴⁹ Ti	1.96×10^{-6}	3.40×10^{-6}	4.77×10^{-6}	5.27×10^{-6}	5.34×10^{-6}	6.74×10^{-6}	1.29×10^{-5}
⁵⁰ Ti	2.47×10^{-11}	6.76×10^{-11}	2.84×10^{-10}	8.4×10^{-7}	5.20×10^{-5}	6.77×10^{-4}	3.68×10^{-3}
⁵⁰ V	1.74×10^{-10}	4.0×10^{-10}	1.44×10^{-9}	6.51×10^{-9}	2.43×10^{-8}	7.21×10^{-8}	1.3×10^{-7}
⁵¹ V	9.23×10^{-6}	1.45×10^{-5}	2.73×10^{-5}	3.60×10^{-5}	6.88×10^{-5}	2.36×10^{-4}	5.16×10^{-4}

Table 4. (cont'd) Mass of major isotopes in the ejecta after all short-lived radioactive isotopes have decayed. The isotope masses are in units of solar mass.

Isotopes	100-133-1-c3-1	200-135-1-c3-1	300-137-1-c3-1	500-138-1-c3-1	550-138-1-c3-1	750-139-1-c3-1	900-140-1-c3-1
⁵⁰ Cr	3.53×10^{-5}	6.40×10^{-5}	1.46×10^{-4}	2.5×10^{-4}	2.19×10^{-4}	2.49×10^{-4}	2.74×10^{-4}
⁵² Cr	7.60×10^{-4}	1.13×10^{-3}	2.1×10^{-3}	3.25×10^{-3}	6.4×10^{-3}	1.25×10^{-2}	1.63×10^{-2}
⁵³ Cr	1.36×10^{-4}	1.94×10^{-4}	4.59×10^{-4}	6.56×10^{-4}	8.40×10^{-4}	1.36×10^{-3}	1.93×10^{-3}
⁵⁴ Cr	1.14×10^{-8}	3.74×10^{-8}	1.47×10^{-6}	2.22×10^{-5}	6.20×10^{-4}	5.33×10^{-3}	1.99×10^{-2}
⁵⁵ Mn	2.56×10^{-3}	3.29×10^{-3}	7.18×10^{-3}	9.3×10^{-3}	1.1×10^{-2}	1.27×10^{-2}	1.53×10^{-2}
⁵⁴ Fe	2.5×10^{-2}	2.89×10^{-2}	7.40×10^{-2}	9.76×10^{-2}	1.5×10^{-1}	1.16×10^{-1}	1.23×10^{-1}
⁵⁶ Fe	2.32×10^{-1}	2.42×10^{-1}	3.49×10^{-1}	3.55×10^{-1}	3.62×10^{-1}	4.8×10^{-1}	4.46×10^{-1}
⁵⁷ Fe	7.41×10^{-3}	7.65×10^{-3}	1.20×10^{-2}	1.22×10^{-2}	1.24×10^{-2}	1.38×10^{-2}	1.57×10^{-2}
⁵⁸ Fe	3.53×10^{-8}	9.64×10^{-8}	2.73×10^{-6}	1.13×10^{-4}	2.34×10^{-3}	1.42×10^{-2}	3.86×10^{-2}
⁶⁰ Fe	1.60×10^{-20}	5.82×10^{-20}	4.49×10^{-17}	4.39×10^{-11}	4.54×10^{-9}	1.14×10^{-7}	1.53×10^{-5}
⁵⁹ Co	1.26×10^{-4}	1.19×10^{-4}	4.5×10^{-4}	5.85×10^{-4}	7.6×10^{-4}	1.1×10^{-3}	1.26×10^{-3}
⁵⁸ Ni	2.13×10^{-2}	2.36×10^{-2}	4.69×10^{-2}	5.47×10^{-2}	5.69×10^{-2}	6.11×10^{-2}	6.44×10^{-2}
⁶⁰ Ni	7.6×10^{-4}	6.97×10^{-4}	3.25×10^{-3}	5.45×10^{-3}	6.76×10^{-3}	8.81×10^{-3}	1.5×10^{-2}
⁶¹ Ni	2.45×10^{-5}	2.11×10^{-5}	3.93×10^{-5}	3.31×10^{-5}	4.75×10^{-5}	8.95×10^{-5}	1.72×10^{-4}
⁶² Ni	2.11×10^{-4}	1.74×10^{-4}	2.79×10^{-4}	2.94×10^{-4}	1.10×10^{-3}	4.26×10^{-3}	8.59×10^{-3}
⁶⁴ Ni	8.88×10^{-15}	1.84×10^{-12}	3.4×10^{-12}	3.60×10^{-8}	2.36×10^{-6}	4.16×10^{-5}	1.34×10^{-3}
⁶³ Cu	1.47×10^{-7}	1.8×10^{-7}	2.31×10^{-7}	2.53×10^{-7}	7.61×10^{-7}	3.76×10^{-6}	1.95×10^{-5}
⁶⁵ Cu	5.51×10^{-8}	4.91×10^{-8}	1.40×10^{-7}	7.48×10^{-8}	1.17×10^{-7}	4.96×10^{-7}	3.0×10^{-6}
⁶⁴ Zn	4.29×10^{-7}	3.68×10^{-7}	9.7×10^{-7}	6.43×10^{-7}	5.93×10^{-7}	8.88×10^{-7}	1.25×10^{-6}
⁶⁶ Zn	9.51×10^{-7}	8.1×10^{-7}	1.72×10^{-6}	1.12×10^{-6}	1.1×10^{-6}	1.67×10^{-6}	2.50×10^{-5}
⁶⁷ Zn	5.57×10^{-10}	4.61×10^{-10}	1.37×10^{-9}	6.64×10^{-10}	1.88×10^{-9}	3.4×10^{-9}	1.15×10^{-6}
⁶⁸ Zn	2.14×10^{-10}	4.97×10^{-10}	5.35×10^{-10}	3.13×10^{-10}	6.52×10^{-9}	3.70×10^{-8}	4.43×10^{-7}
⁷⁰ Zn	1.77×10^{-22}	1.51×10^{-12}	5.64×10^{-22}	1.24×10^{-15}	1.41×10^{-10}	1.73×10^{-11}	7.49×10^{-8}

Table 5. Masses of the radioactive isotopes in the ejecta after the explosion. The isotope masses are in units of solar mass.

Isotopes	100-133-1-c3-1	200-135-1-c3-1	300-137-1-c3-1	500-138-1-c3-1	550-138-1-c3-1	750-139-1-c3-1	900-140-1-c3-1
²² Na	2.29×10^{-9}	9.80×10^{-9}	1.6×10^{-8}	1.0×10^{-8}	9.79×10^{-9}	2.62×10^{-8}	3.66×10^{-8}
²⁶ Al	1.11×10^{-6}	4.61×10^{-6}	4.82×10^{-6}	5.12×10^{-6}	4.85×10^{-6}	1.22×10^{-5}	1.69×10^{-5}
³⁹ Ar	7.40×10^{-10}	2.13×10^{-9}	2.2×10^{-9}	1.94×10^{-9}	2.1×10^{-9}	6.51×10^{-9}	9.2×10^{-9}
⁴⁰ K	3.91×10^{-9}	1.11×10^{-8}	1.4×10^{-8}	9.70×10^{-9}	1.5×10^{-8}	3.33×10^{-8}	4.42×10^{-8}
⁴¹ Ca	4.29×10^{-7}	1.0×10^{-6}	1.23×10^{-6}	8.93×10^{-7}	1.11×10^{-6}	1.15×10^{-6}	1.46×10^{-6}
⁴⁴ Ti	8.12×10^{-7}	1.64×10^{-6}	1.74×10^{-6}	1.51×10^{-6}	1.52×10^{-6}	1.68×10^{-6}	1.81×10^{-6}
⁴⁸ V	3.94×10^{-9}	8.54×10^{-9}	1.5×10^{-8}	8.45×10^{-9}	1.2×10^{-8}	1.24×10^{-8}	1.63×10^{-8}
⁴⁹ V	8.9×10^{-9}	4.31×10^{-8}	9.30×10^{-8}	1.20×10^{-7}	1.57×10^{-7}	2.21×10^{-7}	2.80×10^{-7}
⁵³ Mn	3.43×10^{-6}	1.61×10^{-4}	3.67×10^{-4}	4.60×10^{-4}	5.51×10^{-4}	5.96×10^{-4}	6.99×10^{-4}
⁶⁰ Fe	2.48×10^{-19}	6.76×10^{-16}	6.14×10^{-10}	6.36×10^{-8}	1.52×10^{-7}	1.59×10^{-6}	2.25×10^{-4}
⁵⁶ Co	1.96×10^{-5}	7.1×10^{-5}	1.0×10^{-4}	1.9×10^{-4}	1.11×10^{-4}	1.23×10^{-4}	1.30×10^{-4}
⁵⁷ Co	2.39×10^{-5}	6.48×10^{-4}	1.26×10^{-3}	1.45×10^{-3}	1.57×10^{-3}	1.71×10^{-3}	1.93×10^{-3}
⁶⁰ Co	9.31×10^{-14}	5.13×10^{-11}	1.94×10^{-8}	3.3×10^{-7}	6.8×10^{-7}	1.58×10^{-6}	4.3×10^{-6}
⁵⁶ Ni	2.32×10^{-1}	3.9×10^{-1}	3.21×10^{-1}	3.8×10^{-1}	3.1×10^{-1}	3.18×10^{-1}	3.39×10^{-1}
⁵⁷ Ni	7.39×10^{-3}	1.4×10^{-2}	1.9×10^{-2}	1.6×10^{-2}	1.5×10^{-2}	1.11×10^{-2}	1.21×10^{-2}
⁵⁹ Ni	1.64×10^{-5}	2.36×10^{-4}	4.36×10^{-4}	4.89×10^{-4}	5.13×10^{-4}	5.63×10^{-4}	6.31×10^{-4}
⁶³ Ni	1.96×10^{-15}	3.20×10^{-12}	1.41×10^{-8}	3.73×10^{-7}	8.4×10^{-7}	2.84×10^{-6}	1.70×10^{-5}

Table 6. Mass of major isotopes in the ejecta after all short-lived radioactive isotopes have decayed. The isotope masses are in units of solar mass.

Isotopes	100-043-1-c3	200-045-1-c3	300-047-1-c3	500-048-1-c3	550-048-1-c3	750-049-1-c3	900-050-1-c3
¹² C	1.32×10^{-1}	1.39×10^{-1}	1.34×10^{-1}	1.18×10^{-1}	1.23×10^{-1}	1.4×10^{-1}	9.35×10^{-2}
¹³ C	7.21×10^{-12}	1.95×10^{-11}	2.42×10^{-11}	3.0×10^{-11}	2.20×10^{-11}	3.16×10^{-11}	2.63×10^{-11}
¹⁴ N	2.76×10^{-9}	7.6×10^{-9}	8.29×10^{-9}	1.1×10^{-8}	7.29×10^{-9}	1.7×10^{-8}	1.8×10^{-8}
¹⁵ N	3.31×10^{-7}	5.52×10^{-7}	5.86×10^{-7}	6.42×10^{-7}	5.66×10^{-7}	7.33×10^{-7}	8.57×10^{-7}
¹⁶ O	3.63×10^{-1}	3.92×10^{-1}	3.80×10^{-1}	3.41×10^{-1}	3.52×10^{-1}	3.8×10^{-1}	2.85×10^{-1}
¹⁷ O	6.1×10^{-11}	1.67×10^{-10}	2.4×10^{-10}	2.53×10^{-10}	1.77×10^{-10}	2.54×10^{-10}	2.30×10^{-10}
¹⁸ O	2.89×10^{-12}	7.78×10^{-12}	9.52×10^{-12}	1.16×10^{-11}	8.20×10^{-12}	1.17×10^{-11}	1.5×10^{-11}
¹⁹ F	1.8×10^{-10}	2.68×10^{-10}	3.24×10^{-10}	4.1×10^{-10}	2.88×10^{-10}	4.1×10^{-10}	3.74×10^{-10}
²⁰ Ne	2.16×10^{-1}	2.29×10^{-1}	2.22×10^{-1}	1.97×10^{-1}	2.5×10^{-1}	1.75×10^{-1}	1.57×10^{-1}
²¹ Ne	4.79×10^{-9}	1.6×10^{-8}	1.28×10^{-8}	1.57×10^{-8}	1.17×10^{-8}	1.55×10^{-8}	1.64×10^{-8}
²² Ne	8.38×10^{-9}	1.74×10^{-8}	2.6×10^{-8}	2.52×10^{-8}	1.96×10^{-8}	2.49×10^{-8}	2.79×10^{-8}
²³ Na	2.68×10^{-6}	4.68×10^{-6}	5.61×10^{-6}	6.65×10^{-6}	5.65×10^{-6}	6.72×10^{-6}	7.73×10^{-6}
²⁴ Mg	3.61×10^{-3}	5.60×10^{-3}	5.90×10^{-3}	6.90×10^{-3}	5.75×10^{-3}	7.22×10^{-3}	7.65×10^{-3}
²⁵ Mg	8.84×10^{-8}	1.64×10^{-7}	1.92×10^{-7}	2.30×10^{-7}	1.86×10^{-7}	2.28×10^{-7}	2.58×10^{-7}
²⁶ Mg	7.73×10^{-7}	1.34×10^{-6}	1.61×10^{-6}	1.89×10^{-6}	1.72×10^{-6}	1.93×10^{-6}	2.22×10^{-6}
²⁶ Al	2.49×10^{-29}	2.88×10^{-29}	2.99×10^{-29}	4.65×10^{-28}	3.27×10^{-29}	4.44×10^{-28}	3.45×10^{-29}
²⁷ Al	2.34×10^{-5}	3.45×10^{-5}	3.76×10^{-5}	4.74×10^{-5}	3.91×10^{-5}	4.87×10^{-5}	4.57×10^{-5}
²⁸ Si	2.42×10^{-2}	3.40×10^{-2}	3.61×10^{-2}	3.76×10^{-2}	3.36×10^{-2}	3.73×10^{-2}	3.66×10^{-2}
²⁹ Si	6.79×10^{-6}	1.11×10^{-5}	1.11×10^{-5}	1.21×10^{-5}	1.6×10^{-5}	1.32×10^{-5}	1.55×10^{-5}
³⁰ Si	4.38×10^{-6}	6.99×10^{-6}	7.42×10^{-6}	8.52×10^{-6}	7.17×10^{-6}	9.24×10^{-6}	1.3×10^{-5}
³¹ P	1.45×10^{-5}	2.23×10^{-5}	2.35×10^{-5}	2.59×10^{-5}	2.22×10^{-5}	2.84×10^{-5}	2.95×10^{-5}
³² S	1.32×10^{-2}	1.78×10^{-2}	1.89×10^{-2}	2.1×10^{-2}	1.80×10^{-2}	1.95×10^{-2}	1.81×10^{-2}
³³ S	4.24×10^{-6}	7.37×10^{-6}	7.31×10^{-6}	7.78×10^{-6}	6.87×10^{-6}	9.28×10^{-6}	1.19×10^{-5}
³⁴ S	1.75×10^{-7}	3.7×10^{-7}	3.61×10^{-7}	4.0×10^{-7}	3.34×10^{-7}	5.5×10^{-7}	6.83×10^{-7}
³⁶ S	2.84×10^{-13}	4.9×10^{-13}	4.78×10^{-13}	3.15×10^{-12}	4.30×10^{-12}	1.32×10^{-10}	3.94×10^{-10}
³⁵ Cl	7.15×10^{-7}	1.6×10^{-6}	1.16×10^{-6}	1.29×10^{-6}	1.13×10^{-6}	1.50×10^{-6}	1.66×10^{-6}
³⁷ Cl	2.86×10^{-7}	5.3×10^{-7}	5.38×10^{-7}	5.22×10^{-7}	5.7×10^{-7}	7.12×10^{-7}	8.88×10^{-7}
³⁶ Ar	2.59×10^{-3}	3.45×10^{-3}	3.63×10^{-3}	3.98×10^{-3}	3.56×10^{-3}	3.90×10^{-3}	3.58×10^{-3}
³⁸ Ar	2.42×10^{-8}	4.18×10^{-8}	4.88×10^{-8}	6.49×10^{-8}	6.66×10^{-8}	1.13×10^{-7}	1.48×10^{-7}
⁴⁰ Ar	7.5×10^{-17}	1.28×10^{-16}	1.49×10^{-16}	4.89×10^{-13}	7.4×10^{-13}	1.45×10^{-11}	3.79×10^{-11}
³⁹ K	1.29×10^{-7}	1.82×10^{-7}	1.99×10^{-7}	2.43×10^{-7}	2.17×10^{-7}	2.80×10^{-7}	3.28×10^{-7}
⁴⁰ K	9.7×10^{-14}	1.67×10^{-13}	1.94×10^{-13}	3.55×10^{-13}	3.70×10^{-13}	6.85×10^{-13}	1.1×10^{-12}
⁴¹ K	4.3×10^{-8}	7.64×10^{-8}	9.20×10^{-8}	7.1×10^{-8}	8.9×10^{-8}	9.62×10^{-8}	1.3×10^{-7}
⁴⁰ Ca	2.37×10^{-3}	3.10×10^{-3}	3.23×10^{-3}	3.66×10^{-3}	3.29×10^{-3}	3.62×10^{-3}	3.28×10^{-3}
⁴² Ca	1.38×10^{-10}	2.44×10^{-10}	3.59×10^{-10}	3.81×10^{-9}	4.8×10^{-9}	7.81×10^{-9}	1.1×10^{-8}
⁴³ Ca	2.18×10^{-9}	2.30×10^{-9}	2.52×10^{-9}	3.38×10^{-9}	2.80×10^{-9}	3.35×10^{-9}	7.76×10^{-9}
⁴⁴ Ca	1.47×10^{-6}	2.4×10^{-6}	2.20×10^{-6}	2.91×10^{-6}	2.55×10^{-6}	2.99×10^{-6}	2.93×10^{-6}
⁴⁶ Ca	1.36×10^{-23}	5.99×10^{-22}	4.97×10^{-22}	3.4×10^{-11}	4.80×10^{-11}	4.23×10^{-9}	2.3×10^{-8}
⁴⁸ Ca	1.84×10^{-25}	2.13×10^{-25}	2.21×10^{-25}	1.41×10^{-12}	3.0×10^{-12}	3.45×10^{-9}	6.64×10^{-7}
⁴⁵ Sc	3.18×10^{-9}	6.8×10^{-9}	8.62×10^{-9}	1.4×10^{-8}	1.5×10^{-8}	1.25×10^{-8}	1.34×10^{-8}
⁴⁶ Ti	7.17×10^{-9}	2.27×10^{-8}	3.85×10^{-8}	1.50×10^{-7}	1.58×10^{-7}	2.52×10^{-7}	3.5×10^{-7}
⁴⁷ Ti	6.93×10^{-9}	1.15×10^{-8}	1.53×10^{-8}	2.77×10^{-8}	2.66×10^{-8}	3.74×10^{-8}	5.16×10^{-8}
⁴⁸ Ti	3.97×10^{-5}	5.47×10^{-5}	5.89×10^{-5}	7.91×10^{-5}	7.27×10^{-5}	8.43×10^{-5}	8.19×10^{-5}
⁴⁹ Ti	9.54×10^{-7}	2.4×10^{-6}	2.85×10^{-6}	4.68×10^{-6}	4.48×10^{-6}	5.67×10^{-6}	8.63×10^{-6}
⁵⁰ Ti	1.18×10^{-19}	8.2×10^{-15}	7.8×10^{-15}	6.73×10^{-6}	1.0×10^{-5}	4.65×10^{-4}	1.89×10^{-3}
⁵⁰ V	3.45×10^{-13}	2.17×10^{-12}	4.39×10^{-12}	4.64×10^{-9}	7.17×10^{-9}	4.23×10^{-8}	7.73×10^{-8}
⁵¹ V	3.25×10^{-6}	9.61×10^{-6}	1.48×10^{-5}	3.59×10^{-5}	3.82×10^{-5}	1.60×10^{-4}	3.45×10^{-4}

Table 7. (cont'd) Mass of major isotopes in the ejecta after all short-lived radioactive isotopes have decayed. The isotope masses are in units of solar mass.

Isotopes	100-043-1-c3	200-045-1-c3	300-047-1-c3	500-048-1-c3	550-048-1-c3	750-049-1-c3	900-050-1-c3
⁵⁰ Cr	8.78×10^{-6}	3.0×10^{-5}	5.36×10^{-5}	1.58×10^{-4}	1.65×10^{-4}	2.24×10^{-4}	2.51×10^{-4}
⁵² Cr	8.67×10^{-4}	1.47×10^{-3}	1.80×10^{-3}	3.69×10^{-3}	4.2×10^{-3}	9.85×10^{-3}	1.48×10^{-2}
⁵³ Cr	6.70×10^{-5}	1.64×10^{-4}	2.34×10^{-4}	5.77×10^{-4}	6.3×10^{-4}	1.13×10^{-3}	1.66×10^{-3}
⁵⁴ Cr	4.87×10^{-11}	2.61×10^{-9}	5.32×10^{-9}	9.13×10^{-5}	1.32×10^{-4}	3.53×10^{-3}	1.13×10^{-2}
⁵⁵ Mn	1.5×10^{-3}	2.52×10^{-3}	3.64×10^{-3}	7.85×10^{-3}	7.93×10^{-3}	1.13×10^{-2}	1.37×10^{-2}
⁵⁴ Fe	7.18×10^{-3}	2.6×10^{-2}	3.50×10^{-2}	8.58×10^{-2}	8.94×10^{-2}	1.11×10^{-1}	1.18×10^{-1}
⁵⁶ Fe	1.82×10^{-1}	2.42×10^{-1}	2.78×10^{-1}	3.78×10^{-1}	3.55×10^{-1}	4.13×10^{-1}	4.56×10^{-1}
⁵⁷ Fe	3.40×10^{-3}	4.99×10^{-3}	6.8×10^{-3}	9.29×10^{-3}	8.86×10^{-3}	1.5×10^{-2}	1.18×10^{-2}
⁵⁸ Fe	1.19×10^{-10}	8.82×10^{-9}	2.6×10^{-8}	3.73×10^{-4}	5.34×10^{-4}	9.16×10^{-3}	2.45×10^{-2}
⁶⁰ Fe	2.71×10^{-26}	9.96×10^{-22}	6.64×10^{-22}	5.21×10^{-10}	7.15×10^{-10}	9.73×10^{-8}	6.26×10^{-6}
⁵⁹ Co	2.43×10^{-5}	3.38×10^{-5}	4.88×10^{-5}	3.59×10^{-4}	3.94×10^{-4}	7.49×10^{-4}	9.97×10^{-4}
⁵⁸ Ni	5.35×10^{-3}	1.10×10^{-2}	1.74×10^{-2}	3.85×10^{-2}	4.0×10^{-2}	4.74×10^{-2}	4.96×10^{-2}
⁶⁰ Ni	8.3×10^{-4}	8.46×10^{-4}	9.47×10^{-4}	3.88×10^{-3}	4.17×10^{-3}	7.81×10^{-3}	1.0×10^{-2}
⁶¹ Ni	1.50×10^{-5}	1.54×10^{-5}	1.69×10^{-5}	2.42×10^{-5}	2.36×10^{-5}	5.79×10^{-5}	1.9×10^{-4}
⁶² Ni	2.67×10^{-5}	2.24×10^{-5}	2.30×10^{-5}	1.74×10^{-4}	2.40×10^{-4}	2.56×10^{-3}	5.86×10^{-3}
⁶⁴ Ni	7.9×10^{-18}	2.33×10^{-15}	3.55×10^{-15}	3.9×10^{-7}	4.61×10^{-7}	3.44×10^{-5}	5.98×10^{-4}
⁶³ Cu	6.64×10^{-8}	6.7×10^{-8}	7.31×10^{-8}	1.99×10^{-7}	2.37×10^{-7}	2.43×10^{-6}	1.1×10^{-5}
⁶⁵ Cu	3.87×10^{-8}	4.7×10^{-8}	4.43×10^{-8}	6.7×10^{-8}	5.74×10^{-8}	3.17×10^{-7}	1.49×10^{-6}
⁶⁴ Zn	4.53×10^{-6}	5.42×10^{-6}	6.10×10^{-6}	7.93×10^{-6}	6.72×10^{-6}	7.68×10^{-6}	8.76×10^{-6}
⁶⁶ Zn	1.34×10^{-7}	1.18×10^{-7}	1.28×10^{-7}	1.44×10^{-7}	1.27×10^{-7}	2.12×10^{-7}	8.84×10^{-6}
⁶⁷ Zn	2.17×10^{-10}	2.81×10^{-10}	3.13×10^{-10}	4.43×10^{-10}	3.83×10^{-10}	2.51×10^{-9}	4.56×10^{-7}
⁶⁸ Zn	7.61×10^{-9}	1.19×10^{-8}	1.26×10^{-8}	1.77×10^{-8}	1.56×10^{-8}	3.61×10^{-8}	2.6×10^{-7}
⁷⁰ Zn	1.94×10^{-27}	7.30×10^{-27}	7.19×10^{-27}	2.29×10^{-14}	3.85×10^{-14}	2.38×10^{-11}	2.88×10^{-8}

Table 8. Masses of the radioactive isotopes in the ejecta after the explosion. The isotope masses are in units of solar mass.

Isotopes	100-043-1-c3	200-045-1-c3	300-047-1-c3	500-048-1-c3	550-048-1-c3	750-049-1-c3	900-050-1-c3
²² Na	7.3×10^{-9}	1.43×10^{-8}	1.69×10^{-8}	2.5×10^{-8}	1.59×10^{-8}	2.2×10^{-8}	2.27×10^{-8}
²⁶ Al	6.45×10^{-7}	1.10×10^{-6}	1.32×10^{-6}	1.55×10^{-6}	1.35×10^{-6}	1.58×10^{-6}	1.84×10^{-6}
³⁹ Ar	7.45×10^{-16}	1.26×10^{-15}	1.47×10^{-15}	4.96×10^{-14}	7.28×10^{-14}	5.30×10^{-13}	1.4×10^{-12}
⁴⁰ K	9.12×10^{-14}	1.68×10^{-13}	1.95×10^{-13}	3.57×10^{-13}	3.72×10^{-13}	6.89×10^{-13}	1.1×10^{-12}
⁴¹ Ca	3.69×10^{-8}	6.54×10^{-8}	7.86×10^{-8}	7.11×10^{-8}	7.61×10^{-8}	9.73×10^{-8}	1.4×10^{-7}
⁴⁴ Ti	1.48×10^{-6}	2.1×10^{-6}	2.17×10^{-6}	2.71×10^{-6}	2.44×10^{-6}	2.80×10^{-6}	2.73×10^{-6}
⁴⁸ V	5.9×10^{-10}	9.69×10^{-10}	1.32×10^{-9}	2.54×10^{-9}	2.54×10^{-9}	3.17×10^{-9}	3.51×10^{-9}
⁴⁹ V	6.40×10^{-11}	2.53×10^{-10}	4.74×10^{-10}	4.2×10^{-8}	5.36×10^{-8}	1.35×10^{-7}	1.99×10^{-7}
⁵³ Mn	9.19×10^{-8}	1.16×10^{-6}	3.15×10^{-6}	2.23×10^{-4}	2.58×10^{-4}	5.35×10^{-4}	7.8×10^{-4}
⁶⁰ Fe	1.32×10^{-25}	1.47×10^{-20}	9.87×10^{-21}	7.47×10^{-9}	1.15×10^{-8}	1.39×10^{-6}	9.9×10^{-5}
⁵⁶ Co	6.46×10^{-6}	1.81×10^{-5}	3.28×10^{-5}	8.57×10^{-5}	9.8×10^{-5}	1.11×10^{-4}	1.19×10^{-4}
⁵⁷ Co	1.18×10^{-6}	1.6×10^{-5}	3.15×10^{-5}	8.72×10^{-4}	9.10×10^{-4}	1.59×10^{-3}	1.88×10^{-3}
⁶⁰ Co	3.96×10^{-17}	2.68×10^{-14}	3.67×10^{-14}	4.90×10^{-8}	7.2×10^{-8}	9.86×10^{-7}	2.60×10^{-6}
⁵⁶ Ni	1.82×10^{-1}	2.42×10^{-1}	2.78×10^{-1}	3.58×10^{-1}	3.30×10^{-1}	3.44×10^{-1}	3.56×10^{-1}
⁵⁷ Ni	3.40×10^{-3}	4.98×10^{-3}	6.5×10^{-3}	8.37×10^{-3}	7.87×10^{-3}	8.38×10^{-3}	8.77×10^{-3}
⁵⁹ Ni	2.8×10^{-6}	9.1×10^{-6}	2.21×10^{-5}	3.8×10^{-4}	3.18×10^{-4}	5.18×10^{-4}	5.91×10^{-4}
⁶³ Ni	1.33×10^{-20}	6.32×10^{-16}	6.26×10^{-16}	5.77×10^{-8}	8.25×10^{-8}	1.94×10^{-6}	9.8×10^{-6}

Table 9. Mass of major isotopes in the ejecta after all short-lived radioactive isotopes have decayed. The isotope masses are in units of solar mass.

Isotopes	800-000-1-c3-1	800-000-1-b1-1	900-000-1-c3-1
¹² C	1.53×10^{-7}	1.29×10^{-7}	1.92×10^{-7}
¹³ C	9.46×10^{-14}	7.52×10^{-14}	9.42×10^{-14}
¹⁴ N	1.77×10^{-9}	8.72×10^{-10}	1.98×10^{-9}
¹⁵ N	3.6×10^{-7}	1.40×10^{-7}	3.27×10^{-7}
¹⁶ O	2.56×10^{-1}	1.37×10^{-1}	1.96×10^{-1}
¹⁷ O	4.86×10^{-12}	1.82×10^{-12}	1.20×10^{-12}
¹⁸ O	3.62×10^{-14}	1.78×10^{-14}	2.80×10^{-14}
¹⁹ F	2.18×10^{-12}	1.12×10^{-12}	1.5×10^{-12}
²⁰ Ne	1.93×10^{-1}	1.5×10^{-1}	1.46×10^{-1}
²¹ Ne	1.72×10^{-8}	7.44×10^{-9}	7.44×10^{-9}
²² Ne	4.72×10^{-8}	2.83×10^{-8}	2.65×10^{-8}
²³ Na	3.53×10^{-8}	1.56×10^{-8}	1.68×10^{-8}
²⁴ Mg	2.8×10^{-3}	9.22×10^{-4}	1.32×10^{-3}
²⁵ Mg	4.53×10^{-9}	1.99×10^{-9}	2.3×10^{-9}
²⁶ Mg	8.90×10^{-9}	6.26×10^{-9}	6.19×10^{-9}
²⁶ Al	3.38×10^{-29}	5.29×10^{-13}	5.21×10^{-13}
²⁷ Al	1.90×10^{-6}	7.24×10^{-7}	1.26×10^{-6}
²⁸ Si	2.58×10^{-2}	2.7×10^{-2}	2.43×10^{-2}
²⁹ Si	6.14×10^{-6}	3.46×10^{-6}	6.32×10^{-6}
³⁰ Si	2.66×10^{-6}	1.74×10^{-6}	3.15×10^{-6}
³¹ P	1.1×10^{-5}	6.8×10^{-6}	9.98×10^{-6}
³² S	1.61×10^{-2}	1.36×10^{-2}	1.52×10^{-2}
³³ S	4.8×10^{-6}	2.35×10^{-6}	4.21×10^{-6}
³⁴ S	9.9×10^{-7}	9.7×10^{-7}	1.19×10^{-6}
³⁶ S	2.30×10^{-10}	1.11×10^{-9}	3.48×10^{-10}
³⁵ Cl	9.93×10^{-7}	7.87×10^{-7}	9.92×10^{-7}
³⁷ Cl	7.12×10^{-7}	4.97×10^{-7}	8.9×10^{-7}
³⁶ Ar	3.57×10^{-3}	3.4×10^{-3}	3.38×10^{-3}
³⁸ Ar	4.60×10^{-7}	3.56×10^{-7}	4.17×10^{-7}
⁴⁰ Ar	2.45×10^{-11}	1.1×10^{-10}	3.61×10^{-11}
³⁹ K	4.86×10^{-7}	3.54×10^{-7}	4.84×10^{-7}
⁴⁰ K	9.60×10^{-13}	1.42×10^{-12}	1.34×10^{-12}
⁴¹ K	1.60×10^{-7}	1.20×10^{-7}	1.75×10^{-7}
⁴⁰ Ca	3.61×10^{-3}	3.4×10^{-3}	3.41×10^{-3}
⁴² Ca	4.74×10^{-8}	5.78×10^{-7}	1.82×10^{-7}
⁴³ Ca	3.68×10^{-9}	2.10×10^{-8}	5.77×10^{-9}
⁴⁴ Ca	3.47×10^{-6}	3.0×10^{-6}	3.41×10^{-6}
⁴⁶ Ca	1.2×10^{-8}	7.39×10^{-8}	1.72×10^{-8}
⁴⁸ Ca	2.26×10^{-7}	1.13×10^{-5}	6.94×10^{-7}
⁴⁵ Sc	3.39×10^{-8}	1.5×10^{-7}	7.95×10^{-8}
⁴⁶ Ti	4.18×10^{-7}	5.7×10^{-7}	4.83×10^{-7}
⁴⁷ Ti	5.76×10^{-8}	8.28×10^{-8}	6.37×10^{-8}
⁴⁸ Ti	1.6×10^{-4}	9.43×10^{-5}	1.3×10^{-4}
⁴⁹ Ti	9.34×10^{-6}	2.47×10^{-5}	1.9×10^{-5}
⁵⁰ Ti	9.98×10^{-4}	6.66×10^{-3}	1.62×10^{-3}
⁵⁰ V	7.33×10^{-8}	1.73×10^{-7}	1.1×10^{-7}
⁵¹ V	2.63×10^{-4}	8.73×10^{-4}	3.59×10^{-4}

Table 10. (cont'd) Mass of major isotopes in the ejecta after all short-lived radioactive isotopes have decayed. The isotope masses are in units of solar mass.

Isotopes	800-000-1-c3-1	800-000-1-b1-1	900-000-1-c3-1
⁵⁰ Cr	3.33×10^{-4}	3.69×10^{-4}	3.50×10^{-4}
⁵² Cr	1.57×10^{-2}	2.82×10^{-2}	1.94×10^{-2}
⁵³ Cr	1.76×10^{-3}	3.11×10^{-3}	2.6×10^{-3}
⁵⁴ Cr	6.65×10^{-3}	3.59×10^{-2}	1.2×10^{-2}
⁵⁵ Mn	1.60×10^{-2}	2.14×10^{-2}	1.74×10^{-2}
⁵⁴ Fe	1.50×10^{-1}	1.60×10^{-1}	1.55×10^{-1}
⁵⁶ Fe	4.97×10^{-1}	5.0×10^{-1}	5.9×10^{-1}
⁵⁷ Fe	1.28×10^{-2}	1.45×10^{-2}	1.34×10^{-2}
⁵⁸ Fe	1.61×10^{-2}	7.12×10^{-2}	2.40×10^{-2}
⁶⁰ Fe	2.38×10^{-6}	4.87×10^{-5}	6.4×10^{-6}
⁵⁹ Co	1.11×10^{-3}	1.89×10^{-3}	1.30×10^{-3}
⁵⁸ Ni	6.6×10^{-2}	6.49×10^{-2}	6.29×10^{-2}
⁶⁰ Ni	1.15×10^{-2}	1.55×10^{-2}	1.30×10^{-2}
⁶¹ Ni	9.27×10^{-5}	2.89×10^{-4}	1.25×10^{-4}
⁶² Ni	4.41×10^{-3}	1.57×10^{-2}	6.41×10^{-3}
⁶⁴ Ni	2.52×10^{-4}	3.32×10^{-3}	4.77×10^{-4}
⁶³ Cu	6.2×10^{-6}	4.41×10^{-5}	9.63×10^{-6}
⁶⁵ Cu	7.99×10^{-7}	7.29×10^{-6}	1.37×10^{-6}
⁶⁴ Zn	7.72×10^{-6}	5.86×10^{-6}	7.32×10^{-6}
⁶⁶ Zn	3.24×10^{-6}	1.37×10^{-4}	1.0×10^{-5}
⁶⁷ Zn	1.75×10^{-7}	3.68×10^{-6}	4.27×10^{-7}
⁶⁸ Zn	1.4×10^{-7}	1.2×10^{-6}	1.68×10^{-7}
⁷⁰ Zn	1.5×10^{-8}	3.42×10^{-7}	3.15×10^{-8}

Table 11. Masses of the radioactive isotopes in the ejecta after the explosion. The isotope masses are in units of solar mass.

Isotopes	800-000-1-c3-1	800-000-1-b1-1	900-000-1-c3-1
²² Na	1.71×10^{-10}	1.27×10^{-10}	1.20×10^{-10}
²⁶ Al	2.76×10^{-9}	1.46×10^{-9}	2.58×10^{-9}
³⁹ Ar	8.96×10^{-13}	2.43×10^{-12}	1.25×10^{-12}
⁴⁰ K	9.65×10^{-13}	1.43×10^{-12}	1.35×10^{-12}
⁴¹ Ca	1.54×10^{-7}	1.19×10^{-7}	1.74×10^{-7}
⁴⁴ Ti	3.27×10^{-6}	2.82×10^{-6}	3.22×10^{-6}
⁴⁸ V	5.33×10^{-9}	5.25×10^{-9}	5.40×10^{-9}
⁴⁹ V	2.36×10^{-7}	3.37×10^{-7}	2.82×10^{-7}
⁵³ Mn	8.60×10^{-4}	1.12×10^{-3}	9.63×10^{-4}
⁶⁰ Fe	3.40×10^{-5}	6.84×10^{-4}	8.50×10^{-5}
⁵⁶ Co	1.54×10^{-4}	1.72×10^{-4}	1.63×10^{-4}
⁵⁷ Co	2.32×10^{-3}	2.89×10^{-3}	2.50×10^{-3}
⁶⁰ Co	1.82×10^{-6}	7.75×10^{-6}	2.73×10^{-6}
⁵⁶ Ni	3.83×10^{-1}	3.22×10^{-1}	3.70×10^{-1}
⁵⁷ Ni	9.47×10^{-3}	8.72×10^{-3}	9.43×10^{-3}
⁵⁹ Ni	7.38×10^{-4}	9.3×10^{-4}	7.91×10^{-4}
⁶³ Ni	4.95×10^{-6}	3.65×10^{-5}	7.92×10^{-6}